

TU Delft
Delft University of Technology

Large bone-implants for osteochondral regeneration, fabrication and *ex-vivo* testing.

MSc Thesis

by

Ioanna Gkoni

in partial fulfillment of the requirements for the degree of

Master of Science
Biomedical Engineering,
Specialization: Biomaterials and Tissue Biomechanics,
Faculty of Mechanical, Maritime and Materials Engineering

at the Delft University of Technology,

to be defended publicly on Friday September 25, 2020 at 10:00 AM.

Student number: 4750292

Supervisors:
(Ph.D. Candidate) Mylène de Ruijter
(Assistant Professor Dr. Ir.) Miguel Castilho
(Assistant Professor Dr. Ir.) Mohammad Mirzaali Mazandarani

Exam-committee:
(Professor Dr. Ir.) Amir Zadpoor
(Assistant Professor Dr. Ir.) Angelo Accardo

The thesis is confidential and cannot be made public until 25 September 2025. A electronic version will be available at `https://repository.tudelft.nl/`.

TU Delft Delft University of Technology

Table of Contents

Cover i
Title page ii

Table of Contents iii

List of Figures v

List of Tables viii

List of Abbreviations, (element-) Symbols, and SI units ix
Preface 1

1 Introduction 3
1.1 Current clinical treatments for cartilage regeneration 3
1.2 Physiology and biochemistry of healthy articular cartilage 3
1.3 Tissue engineering for cartilage regeneration 4
1.3.1 Towards Bioprinting 4
1.3.2 Hydrogel use in cartilage regeneration 5
1.3.3 Mechanical reinforcement of hydrogels 5
1.4 Cartilage-bone interface 8
1.5 Tissue engineering for bone regeneration 9
1.6 Tissue engineering for osteochondral regeneration 10
1.7 Ex-vivo models for testing osteochondral implants 11
1.7.1 Available testing machines 11
1.7.2 Comparative biomechanical analysis of human and animal knee models 12
1.8 Conclusions from previous studies 16
1.9 Thesis objective and research aims 16

2 Materials and Methods 17
2.1 Convergence of MEW and extrusion-based techniques 17
2.2 Anatomically shaped implants 17
2.3 Introducing large osteochondral defects 18
2.4 Implants fabrication via FDM 19
2.5 Composite of HB ink 20
2.6 Implants fabrication via pneumatic-driven dispensing 20
2.7 Scaffold fabrication for mechanical testing bulk materials: PCL[1] 22
2.8 Scaffold fabrication for mechanical testing of materials: HB 22
2.9 Mechanical testing of scaffolds 22
2.10 Digital Light Processed *ex-vivo* model 23
2.11 Testing PCL[1]-implants on the DLP *ex-vivo* model 24
2.12 Fusion of PCL[1]-, HB-, and PCL[1]- and HB-fibers 25
2.13 Statistics 26

3 Results 27
3.1 Assessment of the generated Python-code 27
3.2 Fabrication of implants 29
3.3 Mechanical characterization of bulk materials 30
3.4 Mechanical characterization of HB-scaffolds 31
3.4.1 Role of design on scaffolds mechanical behavior 31
3.4.2 Role of chondrogenic differentiation medium on scaffolds mechanical behavior 32

3.5 DLP *ex-vivo* model . . . 33
3.6 Deformation of implants in the DLP *ex-vivo* model . . . 33
3.7 Microscopical characteristics of fused fibers . . . 38

4 Discussion . . . 41

5 Future Suggestions . . . 43

6 Conclusions . . . 45

7 Acknowledgments . . . 46

8 Conflict of Interest . . . 47

References . . . 48

List of Figures

Fig. 1 The structure, synthesis, and mechanical properties of the osteochondral tissue in a zonal representation [16,17] . . . 4
Fig. 2 Schematic representation of FDM [35] . . . 6
Fig. 3 Schematic representation of MEW technique. Adapted from [41] . . . 7
Fig. 4 Illustration of the one-step printing process. MEW, and extrusion-based bioprinting composing the converged printing. Adapted from [42] . . . 8
Fig. 5 Height difference close to the cross-sections of the MEW-deposited fibers (C), and structural gaps created by broken fibers (D). Adapted from [32] . . . 8
Fig. 6 Inversely to the extruded HB-fiber in ambient conditions (B), dense fibers without evident nano-architecture are observed in case of hot-melt HB-fibers (A). Adapted from [50] . . . 10
Fig. 7 The different types of bilayered scaffolds. I: The two-compartment scaffold for bone and cartilage regeneration, II: The scaffold-free approach for the cartilaginous compartment based on the osseous compartment, III: The single and homogeneous scaffolds, and IV: The single but heterogeneous scaffolds [55] . . . 10
Fig. 8 Schematic representation of the knee joint motions and the established anatomical axes [58] . . . 12
Fig. 9 The robotic six-degrees of freedom mechanical testing system as illustrated by [58] . . . 12
Fig. 10 Knee joint physiology and anatomy of the human (first row), the ovine (second row), and the caprine (third row) model. Adapted from [60] . . . 14
Fig. 11 Geometry of human (on the left) and caprine (on the right) knee. Top: anterior view, middle: lateral view, bottom: oblique view [61] . . . 15
Fig. 12 The flowchart of the developed Python-code . . . 17
Fig. 13 Illustration of the .STL file of a human condyle . . . 18
Fig. 13 Four types of defects and the corresponding implants. A: Isometric view of defect I and implant I (17.87 × 15.05 × 6.22 mm), B: Side view of defect I and implant I (17.87 × 15.05 × 6.22 mm), C: Isometric view of defect II and implant II (19.15 × 9.99 × 6 mm), D: Side view of defect II and implant II (19.15 × 9.99 × 6 mm), E: Isometric view of defect III and implant III (19.12 × 5 × 5.95 mm), F: Side view of defect III and implant III (19.12 × 5 × 5.95 mm), G: Isometric view of defect IV and implant IV (10 × 10 × 6 mm), H: Side view of defect IV and implant IV (10 × 10 × 6 mm), (length×width×height) . . . 19
Fig. 14 Combined designs to generate an osseous compartment with four loops in the periphery and closed top layers. A: Top view of the printing path of the four-looped design, B: Top view of the whole construct of the four-looped design, C: Top view of the printing path of the solid design, D: Top view of the whole construct of the solid design . . . 20
Fig. 15 Creating a porous implant at the implant-native bone interface while maintaining the outer periphery loop at the side of the knee joint space. A: Top view of the printing path of the one-loop design, B: The black cross-lines indicate the deleted parts of the periphery loop, C: Top view of the printing path of the no-loop design . . . 21
Fig. 16 Converged printing path. A: The one-loop design combined with the no-loop one, scaled by 100%, B: The one-loop design combined with the no-loop one, scaled by 100% and 98% respectively, C: The one-loop design combined with the no-loop one, scaled by 100% and 97% respectively, D: The one-loop design combined with the no-loop one, scaled by 100% and 96% respectively . . . 21
Fig. 17 The workflow from fabricating the HB-scaffolds to their compression . . . 23
Fig. 18 Fabricating an anatomically-shaped femur using DLP technique . . . 24
Fig. 19 A: Instron 5967, the universal, static testing system used in the case of the DLP *ex-vivo* model, B: Fixation of the DLP-model on the compression plates . . . 24
Fig. 20 The design of the two HB-rectangles fabricated via pneumatic-driven dispensing to investigate the fusion of MEW-deposited PCL[1]-fibers on top of them. Rectangle A: 19×15×2 mm. Rectangle B: 19×10×2 mm (length×width×height) . . . 25

Fig. 21 Correspondence of the STL-file and the manipulated coordinates in the Python-code. A: Top view of human condyle (STL file), B: Back view of human condyle (STL file), C: Side view of human condyle (STL file), D: Top view of human condyle-Python-code, E: Back view of human condyle-Python-code, F: Side view of human condyle-Python-code. The scale-bar corresponds to 5 mm 28

Fig. 22 The three different types of fabricated implants. A: Top view of implant III-(PCL[1]-shielded), B: Side view of implant III-(PCL[1]-shielded), C: Top view of implant III-(HB-shielded), D: Side view of implant III-(HB-shielded), E: Top view of implant III-(HB-porous), F: Side view of implant III-(HB-porous). The scale-bar corresponds to 5 mm 29

Fig. 23 A: Implant I (HB-shielded), B: Implant II (HB-shielded), C: Implant III (HB-shielded), D: Implant IV (HB-shielded), E: Comparing the percentage of fidelity in terms of size in the three dimensions of the fabricated implants. The scale-bar corresponds to 5 mm. $*$ indicates a significant difference, $p < 0.05$ 30

Fig. 24 A: The recorded force-displacement data were converted into stress-strain data, respectively. B: The Young's modulus elasticity was calculated based on the linear part of the slope of the stress-strain curve (red-marked data) 30

Fig. 25 Bulk properties of PCL[1] and HB materials. The compression elasticity of Young's modulus of the human trabecular bone, based on literature [75], is estimated to range from $1.41 * 10^9$ to $3.47 * 10^9$ Pa. $***$ indicates a significant difference, $p < 0.001$. No outliers were identified in the groups 31

Fig. 26 The Young's modulus elasticity of the bulk scaffolds appears to scatter without a specific tendency relevant to their density 31

Fig. 27 Gross representation of the different fabricated designs ("enclosed", "encircled", "open" sides). A: Top view of undeformed HB-scaffolds. B: Side view of undeformed HB-scaffolds. C: Side view of deformed HB-scaffolds. The scale-bar corresponds to 8 mm 32

Fig. 28 Quantification of the Young's modulus elasticity of HB-scaffolds designed following different patterns. $***$ indicates a significant difference, $p < 0.001$. $*$ indicates a significant difference, $p < 0.05$. No outliers were identified in the groups 32

Fig. 29 The effect of pre-culture of the implant *in-vitro* in chondrogenic differentiation medium. No significant statistical difference was found among the examined groups. No outliers were identified in the groups 33

Fig. 30 The DLP equivalent of defect III and the corresponding PCL[1]-fabricated implant. A: Isometric view of defect III. B: Top view of defect III. The scale-bar corresponds to 5 mm 33

Fig. 31 Formation of the open hysteresis loop. The load-deformation curves of six circles of loading and unloading of the Implant I while being inserted in the DLP *ex-vivo* model. A 55° configuration was used 34

Fig. 32 The fabricated implants present a degree of plasticity. The figure shows the load-deformation curves of six circles of loading and unloading of the Implant I while being inserted in the DLP *ex-vivo* model. All the configurations of flexion are presented. The second repetition at the configuration of 55° of flexion demonstrates constantly smaller values of deformation 34

Fig. 33 Elastic (U_e), and dissipated energy (U_d) in a load cycle 35

Fig. 34 The average normalized elastic energy of the different implants in the three degrees of flexion. $***$ indicates a significant difference, $p < 0.001$. $**$ indicates a significant difference, $p < 0.01$. $*$ indicates a significant difference, $p < 0.05$ 36

Fig. 35 The average normalized dissipated energy of the different implants in the three degrees of flexion. $***$ indicates a significant difference, $p < 0.001$. $**$ indicates a significant difference, $p < 0.01$. $*$ indicates a significant difference, $p < 0.05$ 37

Fig. 36 The contact area decreases as the degree of flexion increases 37

Fig. 37 The contact stress at the maximum force. There was not identified a statistically significant difference among the different implants in the same degrees of flexion. Statistical difference was identified among the different degrees of flexion of the same implant. $***$ indicates a significant difference, $p < 0.001$ 38

Fig. 38 The average height-deformation of the tested implants. No outliers were identified in the groups. No significant statistical difference was found in the examined groups 38

Fig. 39 Microscopical characteristics of the deposited fibers within two different types of samples. (A): Top view of the HB-deposited fibers via pneumatic-driven dispensing, (B): Side view of the HB-deposited fibers via pneumatic-driven dispensing, (C): Top view of the PCL^1-deposited fibers via FDM, (D): Side view of the PCL^1-deposited fibers via FDM. The scale-bars correspond to 100 µm. The applied voltage was set at 5 kV 39
Fig. 40 Microscopical characteristics of the PCL^1 deposited fibers (MEW) on top of a HB-surface (pneumatic-driven dispensing). A: Angled view (45°) of PCL^1-deposited fibers at t=0. The scale-bar corresponds to 300 µm, B: Angled view (45°) of PCL^1-deposited fibers at t=t_2. The scale-bar corresponds to 300 µm, C: Angled view (45°) of PCL^1-deposited fibers at t=0. The scale-bar corresponds to 50 µm, D: Angled view (45°) of PCL^1-deposited fibers at t=t_2. The scale-bar corresponds to 80 µm, E: Angled view (45°) of PCL^1-deposited fibers at t=t_2. The scale-bar corresponds to 10 µm, F: Angled view (45°) of PCL^1-deposited fibers at t=t_1. The scale-bar corresponds to 20 µm, The applied voltage was set at 10 kV 40

List of Tables

Table 1 Grading of anatomical similarity of different animal models with human knee. (+) good, (∘) adequate, (-) no similarity in absolute, normalized sizes, and anatomical features with the human one. Adapted from [60] 13
Table 2 Measurements of the range of motion in different knee models. Adapted from [60] 13
Table 3 Printing parameters of the HB- and PCL[1]-deposited fibers 25
Table 4 Numerical validation of Python-code 28
Table 5 Percentage of accuracy of the generated G-code 28
Table 6 Internal architecture of the fabricated implants 29
Table 7 Average displacement(mm) at the maximum force for the defective femur to the tibia configuration, with the implant placement 35
Table 8 Energy ratios. The average total energy (U), the average ratios of the elastic energy (U_e), and the dissipated energy (U_d) per loading/unloading circle. The outliers were removed to calculate the average values 36

List of Abbreviations, (element-) Symbols, and SI units

Abbreviation/Symbol	Explanation
ACI	Autologous Chondrocyte Implantation
ACL	Anterior Cruciate Ligament
BMP	Bone Morphogenetic Proteins
BMSCs	Bone Marrow Stromal Cells
BW	Body-Weight
CaudLB	Caudolateral Bundle
CT	Computed Tomography
CTS	Critical Translation Speed
CraCL	Cranial Cruciate Ligament
CraMB	Craniomedial Bundle
$\mathbf{d_{PD}}$	Translation in the proximal-distal direction
$\mathbf{d_{ML}}$	Translation in the medial-lateral direction
$\mathbf{d_{AP}}$	Translation in the anterior-posterior direction
ECM	Extracellular Matrix
Fe	Iron
FDM	Fuse Deposition Modeling
GAGs	Glycoaminoglycans
GelMA	Gelatin Methactyloyl
GPa	Gigapascal
HA[1]	Hyaluronic Acid
HA[2]	Hydroxyapatite
HB	Hyperelastic Bone
$\mathbf{H_2}$	Hydrogen Gas
$\mathbf{H_2O}$	Water
kPa	Kilopascal
kV	Kilovolt
MEW	Melt Electrowriting
Mg	Magnesium
$\mathbf{Mg(OH)_2}$	Magnesium Hydroxide
$\mathbf{Mg_3(PO_4)_2}$	Magnesium Phosphate
mL	Milliliter
mm	Millimeter
MPa	Megapascal
MRI	Magnetic Resonance Imaging
MSCs	Mesenchymal Stromal Cells
N	Newton
N m	Newton meter
OA	Osteoarthritis
Pa	Pascal
PCL[1]	Polycaprolactone
PCL[2]	Posterior Cruciate Ligament
PDGF	Platelet-Derived Growth Factor
PEG	Poly(ethylene glycol)
PEGDA	Poly(ethylene glycol) Diacrylate
PEGDMA	Poly(ethylene glycol) Dimethacrylate deco-ε-carprolactone)
PLGA	Poly(lactic-co-glycolic acid)
PRG4	Proteoglycan 4
RhBMP-2	Recombinant human Bone Morphological Protein-2
sec	Second
sPEG/Hep	Star-shaped Poly(ethylene-glycol)/Heparin
STL	Standard Tessellation Language
TCP	Tricalcium Phosphate
TE	Tissue Engineering
UFS	Universal Force-moment Sensor
U	Total energy
$\mathbf{U}_d$	Dissipated energy
$\mathbf{U}_e$	Elastic energy
Zn	Zinc
$\mathbf{\Theta_{IE}}$	Internal-external rotation
$\mathbf{\Theta_{FE}}$	Flexion-extension
$\mathbf{\Theta_{VV}}$	Varus-valgus rotation
$\boldsymbol{\mu}$**m**	Micrometer
2D	Two-Dimensional
3D	Three-Dimensional
e.g.	Exampli gratia
°	Degrees
®	Registered Trademark

Preface

The high frequency of osteoarthritis in those aged above 60 years combined with the observing trend of overpopulation leads to increased healthcare costs. To date, clinical treatments seem to be insufficient to restore cartilage and underlying bone degeneration. Bioprinting fabrication techniques constitute a promising approach to mimic and anchor both the biological and mechanical properties of the two different tissues. Moreover, the simultaneous development and junction of an osseous and a cartilaginous compartment would be beneficial to provide mechanical fixation to the latter.

Each tissue, osseous tissue and articular cartilage, presents different physical and mechanical properties. Hence, different biomaterials and bioprinting techniques are commonly used in each case. Therefore, the fusion of an osseous (HB via pneumatic-driven dispensing) and a cartilaginous (PCL[1] via Melt Electro-writing) compartment was investigated in the study. Currently, pneumatic-driven dispensing systems combined with Melt Electro-writing are used to fabricate reinforced hydrogels as a cartilage equivalent. The used techniques are generating constructs using a layer by layer fashion on a flat surface. The possibility to generate the respective constructs on top of a non-smooth and concave surface, such as an osseous implant, was studied in the present work.

Using two different bioprinting techniques, it was possible to fabricate clinically relevant-size bone-implants for osteochondral defects. Firstly, the osseous compartment of the implant was constructed by Fused Method Deposition (FDM) using Polycaprolactone (PCL[1]). Secondly, Hyperelastic "bone" (HB) was chosen based on the osteoinductive properties it shows. Inversely, the HB-implants were fabricated using a pneumatic-driven dispensing system.

Apart from the superior osteoinductive properties of HB over PCL[1], the bulk stiffness of the two materials was measured under uniaxial compression. Following the same protocol, HB-scaffolds with specific internal architecture were evaluated. The different groups of porous HB-scaffolds presented different design details (outer periphery loop and/or closed top layer) to evaluate the impact of each element on the final stiffness. Also, the effect of an *in-vitro* pre-culture period in chondrogenic differentiation medium on the stiffness of the osseous scaffolds was examined.

The gross shape of the osseous compartment may contribute to the fixation of the osteochondral implant. Therefore, multiple types of osseous defects were introduced in the current work. The corresponding implants were fabricated as previously described. The size of the implants and the extent of confinement from the surrounding material were set as the parameters of the study. To evaluate the joint integrity, a Digital Light Processed *ex-vivo* model was fabricated. Particularly, the stifle joint of sheep was chosen as an *ex-vivo* model to replicate the human knee physiology and anatomy. By inserting the fabricated implants into the sites of defects and testing them under the employment of physiological loading conditions, displacement data were acquired.

A Python-code that generates a G-code allowing printing in the transverse plane to that of the building plate was successfully developed. The particular Python-code creates a G-code that enables the print-head to move on top of a concave and non-smooth surface with high accuracy. The results indicate that the Young's modulus elasticity of the osteoinductive HB is lower compared to that of the native trabecular bone. Also, neither the periphery loop nor the closed top layer of the porous HB-scaffolds seem to have a significant impact on the stiffness. The same stands for the pre-culture period in chondrogenic differentiation medium. The *ex-vivo* testing of the fabricated implants indicates that a width of 10 mm might be crucial for the joint integrity. Inversely, the confinement of the implant by the surrounding material seems not to affect it. Finally, the fusion of the osseous and carilaginous compartment appears to be dependent on the material inconsistencies of the bone equivalent. However, porous structures were demonstrated on top of the osseous-surface.

These conclusions could not be reported without the help of my supervisors. Firstly, I would like to thank my daily supervisor, Mylène de Ruijter. Her expertise in bioprinting constituted inspiration to accomplish the main research objectives of the master thesis. Apart from her hard skills, Mylène de Ruijter provided me with her positivity throughout this strained period. Thanks go to the Regenerative Medicine Center of Utrecht for providing its technologically advanced facilities to execute the experimental part of the master thesis. Moreover, I'm also grateful for the instructions of the internal supervisor of TU Delft, Mohammad Mirzaali Mazandarani. His support and good deeds facilitated the process. I would also like to express my gratitude to the rest of the members of the thesis committee, Miguel Castilho and Amir Zadpoor, for their guidance and exchange of arguments. In addition, I am grateful for the support of my family and my friends with whom I shared my anxiety and my ambitions throughout the master's program.

Keywords: biofabrication, osteochondral regeneration, convergence, biomechanics, *ex-vivo*

Ioanna Gkoni
Utrecht, September 2020

Dedicated to the Monday meetings.

Introduction

1.1 Current clinical treatments for cartilage regeneration

Inversely to a few other body tissues (e.g., osseous tissue, skin), articular cartilage does not remodel dynamically through cellular activities. This inability arises from its avascular nature and the low cell density [1]. Therefore, clinical treatments have been developed to cure the populations suffering from articular cartilage-related diseases.

Clinical treatments for cartilage regeneration are of paramount importance considering that approximately 28% of people over the age of 60 are affected by osteoarthritis (OA) [2]. OA is characterized as the end-stage of cartilage's degeneration, leading to friction between the underlying bones. Apart from the high prevalence of OA, due to the severity of the disease it holds a high and reverse impact in the ordinary activities of patients [2]. OA is characterized as a non-symptomatic disease at the very early stages. Inversely, joint pain is demonstrated when cartilage has already lost the inherent viscoelastic properties [3].

To date, the main clinical treatments for focal cartilage defects include the autologous chondrocyte implantation (ACI) and the microfracture. During ACI, chondrocytes are isolated from the articular cartilage of the patient via biopsy. These are expanded *in-vitro* and finally injected under a collagen membrane that is sutured at the place of the defect [4]. The intention of microfracture is to bleed the subchondral bone and, hence, provoke clot formation [5]. Afterwards, inflammatory responses will commence. The treatment selection in each case is based on the size of the osteochondral defect [6]. The technique of microfracture is preferred for small osteochondral defects. Based on a systematic review [7], the ACI technique, appears to have an 82% success rate results in the long-term ($\geq$ nine years). The rate of success is dependent on the age of the patients and the surface area of the defect. Particularly, it can be increased up to 92% in the case of young patients with defects less than 4.5 cm^2. The depth of the defects was not considered as a parameter. The main disadvantage of these clinical treatments is the formation of fibrocartilage, which constitutes an inferior substitute of articular cartilage. Finally, it can even lead to the degeneration of the native articular cartilage and the poorly repaired tissue [8]. However, none of these treatments is suitable for cases where the beingness of the subchondral bone is affected. In that case, total joint arthroplasty is unavoidable. Then, the whole articular cartilage is removed and is replaced by synthetic materials. Regarding this treatment, the main concerns are the long-term pain [9] and the aseptic loosening [10], which can lead to even more complex and expensive revision surgeries [11].

1.2 Physiology and biochemistry of healthy articular cartilage

Cartilage is composed of chondrocytes, the only cell type that we encounter, and the respective extracellular matrix (ECM) which consists of water (≈75%), collagen (mainly type II) (≈15%), and aggrecans (≈10%) [4]. The mechanical properties of each tissue are dependent on the composition of the ECM. In the case of articular cartilage, it is not uniform along the depth of the tissue but it presents a zonal-dependency (Fig.1). Particularly, the collagen fibers represent the tensile strength of cartilage [12], whereas the number of molecules of aggrecans that are located between the collagen fibers affect the water concentration in it. The affinity for water is derived from the negatively charged glycoaminoglycans (GAGs) that are attached to the aggrecan monomers [12]. Hence, GAGs can be characterized as a measure of the compressibility of the tissue [11]. Therefore, articular cartilage in terms of mechanics is a non-linear, anisotropic, biphasic, and viscoelastic material. The solid matrix and the fluid compose the biphasic nature. Its characteristic is that it possesses a low coefficient of friction that enables an almost friction-less articulation in the joints [13]. Although cartilage is characterized by relatively low compressive stiffness (0.1-2 MPa [14]), it is able to withstand stresses that are in the range of a few megapascals. The generating high fluid pressures are responsible for transferring 95% of the stresses. Particularly, the spatial mean contact stress has been calculated to be 2.92 MPa, while the peak local contact stress recorded as 8.80 MPa. Therefore, the solid matrix is compressed to the minimum extent [15].

Briefly, the superficial zone of articular cartilage is characterized by parallel collagen fibers that provide resistance to shear deformations of the tissue. The middle zone comprises the main body of the cartilage's thickness.

There, the collagen fibers do not have a specific orientation, and constitute a bridge toward the deep zone where the fibers are oriented perpendicularly to the bone surface [11]. Respectively to the zonal organization of the collagen fibers, chondrocytes also display zonal variations. Fig.1 illustrates this tissue-specific feature. From the superficial zone to the deep one, a decrease in the cell density is observed while chondrocytes demonstrate the same orientation as the collagen fibers. Moreover, they appear to be flattened in the superficial zone, spherical in the middle one, and spherical, but larger in size, in the deep one [11]. A 13 µm diameter constitutes the average diameter of chondrocytes in the first two zones of articular cartilage. In the deep zone, an increase of up to 20 times has been recorded in the volume of chondrocytes [16].

Respectively, the detected protein expression is different along the depth of the articular cartilage. Particularly, the main markers for the superficial zone are the proteoglycan 4 (PRG4), lubricin, megakaryocyte-stimulating factor, and developmental endothelial locus-1. These markers are not detected in the middle zone, where cartilage intermediate layer protein and Jagged 1 are expressed. The last two markers are also expressed in the deep zone [11]. However, an additional marker is expressed in the cartilage-bone interface (tidemark). There, the cartilage is calcified, meaning that collagen type X is highly expressed [4]. The mechanical properties of that interface are in the range of 0.32±0.25 GPa, providing a gradual transition from the more soft hyaline cartilage (0.24±0.05 MPa) to the more stiff underlying bone (3.9±1.5 GPa) [16].

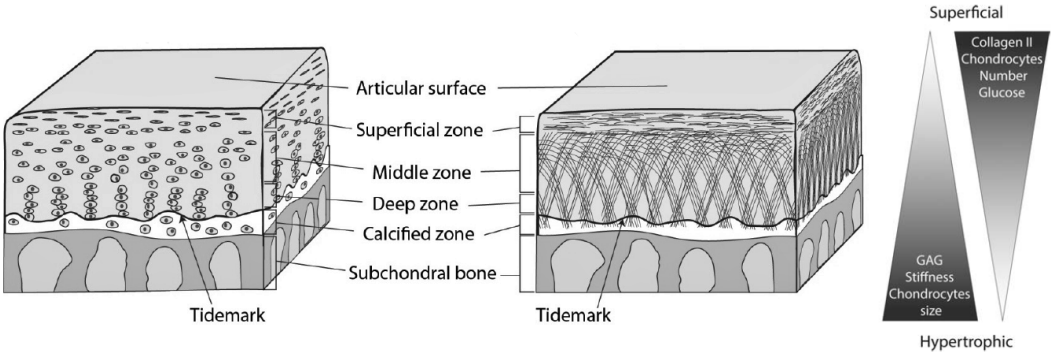


Fig. 1: The structure, synthesis, and mechanical properties of the osteochondral tissue in a zonal representation [16,17]

1.3 Tissue engineering for cartilage regeneration

1.3.1 Towards Bioprinting In contrast to the standard surgical treatments, osteochondral tissue engineering (TE) has emerged as a promising approach. In 1993, TE was originally defined as "*an interdisciplinary field that applies the principles of engineering and life sciences toward the development of biological substitutes that restore, maintain, or improve biological tissue function or a whole organ*" [18]. However, because of the field's broadening, Tissue Science and TE were defined as "*the use of physical, chemical, biological and engineering processes to control and direct the aggregate behavior of cells*" [19].

Among different tissues, the fabrication of cartilage was considered to be a simple engineering process. The basic arguments regarding this statement were the avascular nature, the relatively plain ECM, and the unique cell type, chondrocytes, that resides there [4]. In different approaches, hydrogels have been preferred as biomaterial since they contain high water content (> 90 wt%) [13] that mimics the native tissue of cartilage. However, the zonal-organization of articular cartilage was not considered as a major parameter in the engineered implants. Although this overview led to fabricate implants that mimicked the global mechanical properties of articular cartilage, they failed to withstand the physiological loadings of the knee joint because of the strain discontinuities with the surrounding tissue [11]. For this reason, the interest of TE was focused on engineering implants with zonal mechanical properties.

While subtractive machining techniques were mainly used in the industry, their inability to produce structures with high internal complexity led to the development of three-dimensional (3D) printing, which constitutes an

automated additive technique in which two-dimensional (2D) patterns are stacked in a layer by layer fashion. Since each design is generated by a computer-aided process, the production of unique and complex architectures is controlled and, hence, reproducible [20].

Based on 3D printing, bioprinting was defined as "*the use of computer-aided transfer processes for patterning and assembling living and non-living materials with a prescribed 2D or 3D organization in order to produce bio-engineered structures serving in regenerative medicine, pharmacokinetic and basic cell biology studies*" [21]. Bioprinting allows the generation of 3D cultures that better mimic the cell-cell and the cell-matrix interactions. In multiple *in-vitro* models it has been shown that different cellular responses are stimulated by the same type of cells while they are cultured in 2D and 3D cultures [22].

Compared to the common TE strategies, bioprinting enables the accurate positioning of cells and biochemical cues within a biomaterial [20]. Among the available bioprinting techniques, extrusion-based printing is highly selected in research because of the low cost and the availability of compatible bioinks [23,24,25]. Also, the fabrication speed is a beneficial feature of filament extrusion printing over the inkjet printing and the laser-induced forward transfer. Using extrusion-based systems, it is possible to fabricate clinically-relevant size constructs in a time frame so that cell viability is not adversely affected [26].

1.3.2 Hydrogel use in cartilage regeneration Polymers for bioprinting applications can be classified into two main categories, namely natural and synthetic polymers. The natural polymers (e.g., collagen, chitosan, gelatin) provide biochemical factors that are more native, yet lack the stiffness that is required to achieve the native-like mechanical properties, and reproducibility is not always ensured [27]. Inversely, (biodegradable) synthetic polymers (e.g., PCL[1], poly(ethylene glycol) (PEG), poly(lactic-co-glycolic acid) (PLGA)) show better mechanical properties compared to natural polymers, yet lack the biochemical cues that promote the cell attachment, proliferation, and differentiation [27]. To date, the combination of synthetic and native polymers is of high interest to achieve the optimal cellular responses [20]. The aforementioned properties are not yet optimally combined in one construct. The ultimate goal is to optimize the spatial resolution of different cells' deposition, maintain their viability, stimulate their chondrogenic differentiation, and provide the proper physicochemical cues to promote integration of the implant with the native tissue [28].

Frequently used hydrogels include, collagen and gelatin, gelatin methacryloyl (GelMA), hyaluronic acid (HA[1]), alginate, poly(ethylene glycol) diacrylate (PEGDA), poly(ethylene glycol) dimethacrylate (PEGDMA) and fibrin. However, extrusion-based printing requires these formulations/bioinks to have high printability and, hence, reproducibility, tolerable gelation rate, low cytotoxicity, sufficient mechanical properties, and tuned biodegradability rate. The aforementioned materials have been proven unable to satisfy one or more of these requirements when solely bioprinted [29].

1.3.3 Mechanical reinforcement of hydrogels The hydrogel-based constructs appear to have inferior mechanical properties than those of native articular cartilage. It has been shown that long-term stability of implants is related to their integration with the surrounding tissue at the time of implantation. Generating a fibrous network within hydrogels that can generate the nonlinear, anisotropic, and inhomogeneous properties of articular cartilage is a promising idea as the next step. In the rest of the report, hybrid hydrogels are defined as the hydrogels which are enhanced for mechanical support, usually by thermosensitive polymers.

Klein et al. [30], incorporated the bioprinted hydrogels into FDM-thermoplastic scaffolds. In the same study, it was demonstrated that the mechanical properties of the hydrid hydrogel were tuned by those of the thermoplastic scaffold. This result was independent of the used hydrogel. To adjust the mechanical stiffness of the supporting scaffold, the spacing, the orientation, and the size of the deposited fibers should be optimized [31].

The achieved diameter of the deposited fibers generated by FDM (Fig.2) technologies varies from 100 to 500 µm [32]. However, the need for greater control of the architecture of the produced scaffold set the evolution of the FDM technology [32]. To mimic the anisotropic extracellular environment, technologies that are able to generate structures in the scale of a few μm are essential. Another disadvantage of polymers' extrusion in FDM is their potential degradation because of the applied shear stresses at the nozzles [32].

Melt Electro-writing (MEW) (Fig.3) has been used to generate thinner fibers. While in FDM the diameter of the fiber is dependent on the inner diameter of the nozzle, during electro-writing the fiber is actually drawn by

the electrostatical force and, hence, the diameter of the fiber is decreased up to 100 times. To ensure that the jet is deposited accurately, the molten jet should be electrically stable and show a minimal jet lag while writing. To obtain straight jets in melt electro-writing, the collector plate or the nozzle, depending on which part is translating in each MEW configuration, should be moving at speeds that are compatible with the speed of the jet [33]. Based on the same study, the printing parameters for a specific material that should be optimized with respect to each other are the melt temperature, the extrusion rate, the applied voltage, and the collector distance. The spinneret size was considered to be constant. In general, the generated fibers have diameters that usually range from 5 to 30 µm [32]. As far as the cell adhesion is concerned, the thinnest fibers are optimal. However, manipulating thin fibers of 3-5 µm is not convenient. Also, their fidelity is probably more susceptible to deformations during mechanical testing and physiological loading conditions [34].

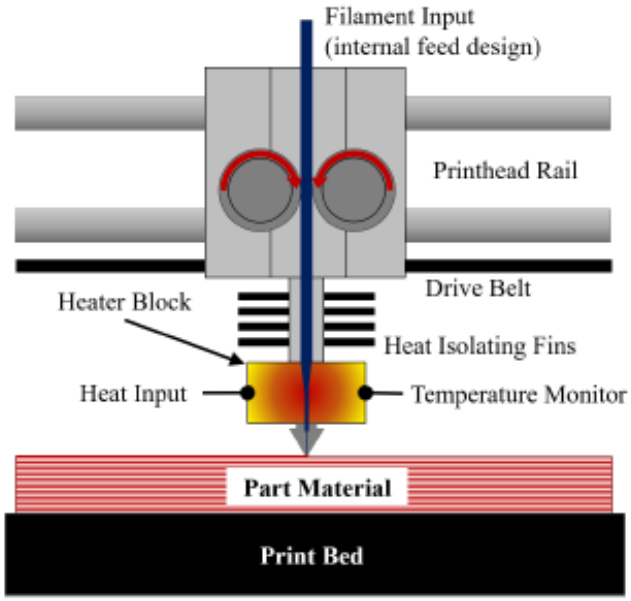


Fig. 2: Schematic representation of FDM [35]

PCL[1] melt electrowritten fibers have already been combined with numerous types of hydrogels. The specific material is safe to be exposed to body temperature. The glass-transition temperature of -60°C, ensures that the raw mechanical properties will not be altered *in-vivo*. Also, it is chemically stable since it has a decomposition temperature of 350°C [36]. PCL[1] can maintain the mechanical integrity for 5 to 6 months and then it degrades evenly within 24 months [37]. Hence, it provides the desired support to cells until the new-formed tissue is mature enough.

Onur et al. [38] used star-shaped poly(ethylene glycol)/heparin hydrogel (sPEG/Hep) to examine their mechanical reinforcement by a MEW-fabricated thermosensitive polymer. It was proved that the PCL[1]-made fibrous network provided appropriate microenvironment toward the differentiation of chondrocytes. Particularly, the marker genes of aggrecan, collagen type II, and PRG4 were up-regulated compared to the sPEG/Hep hydrogels alone. Collagen type I presented the same expression levels in both types of scaffolds. Also, the mechanical stiffness was increased by forty-two times. The reinforced compressive modulus was recorded as 1497.05 ± 138.26 kPa, while, in the experiments of human articular cartilage, a value of 1629.30 ± 256.48 kPa was reported. A fifty-four times higher stiffness in the hybrid scaffolds (reaching a reinforced value of 405 ± 68 kPa) compared to the hydrogels alone was reported in another study [39]. In a study by Mouser et al. [1], the hybrid scaffolds experienced three orders of magnitude greater mechanical stiffness (reaching a reinforced value of 3500-4600 kPa) compared to the non-reinforced scaffolds. Another study [40] presented a thirty-eight times increase of the elastic Young's modulus

in the case of reinforced hydrogels (reaching a reinforced value of 645 ± 12 kPa). Similarly, they concluded that the mechanical properties of the hybrid scaffolds were tuned mainly by the mechanical properties of the supporting (PCL[1]) scaffold. The difference in the degree of the achieved reinforcement among the aforementioned studies can be attributed to the different geometries of the supporting scaffolds. As it has been proven the fiber spacing, the fiber size, and the fiber orientation are capable of tailoring the stiffness of the PCL[1] construct. Since the mechanical properties of hybrid scaffolds are tuned by the supporting scaffold, then the density of the cross-linker can be decreased to favor the cellular activities.

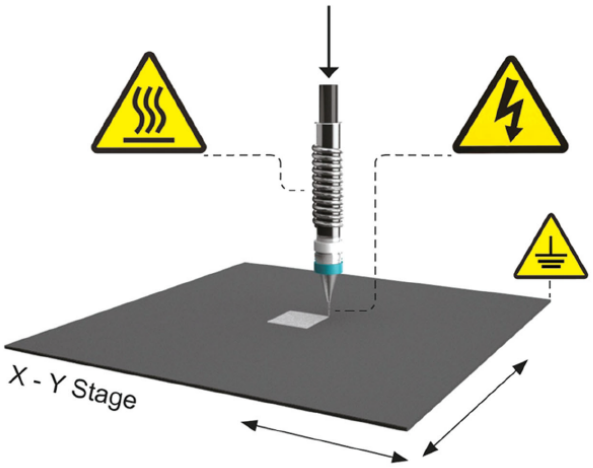


Fig. 3: Schematic representation of MEW technique. Adapted from [41]

However, that high temperatures that are used to get the thermosensitive polymer molten are not cell-friendly. For this reason, the encapsulation of cells in MEW scaffolds is done by infiltrating the cell-laden hydrogel into the thermosensitive scaffold. This process is characterized as a two-step procedure. The disadvantage of this is that it hinders the incorporation of different materials, and cell types in the final hybrid scaffold [42]. Hence, the capability of mimicking the hierarchical architecture of native tissue is limited. In an interesting study, it was possible to merge these two different additive manufacturing techniques (Fig.4) [42]. The hybrid scaffolds made by the one-step (converged) printing procedure and the two-step (conventional) one were compared in terms of their mechanical properties, the cell viability, and the cell differentiation toward the chondrogenic lineage. It was concluded that the mechanical stiffness was not affected by the modification of the printing process. Moreover, neither the larger fabrication time nor the applied high voltage (up to 15 kV) had a significant impact on the cell viability, and the ECM formation.

In the same study [42], in addition to providing reinforcement in terms of the mechanical properties, PCL[1] scaffold was also used to achieve a more controllable deposition of the cell-laden GelMA. Combining MEW, and bioprinting allows the pores of the PCL[1] construct to create physical boundaries and to position the bioink with high accuracy.

A disadvantage of MEW is the final thickness of the generated structures. The height of the structure, and the periodicity are correlated by an adverse fashion. In an interesting study [32], it was demonstrated that the height of the squared-patterned scaffold is maximized at the intersection of the fibers. This resulted to the development of structural discontinuities that were more intense with increasing the height. Fig.5 presents these observations. These structural defects were localized at a height of 24-32 µm. Hence, up-scaling of these scaffolds is limited by their mechanical instabilities. Increased height of the scaffold at the cross-sections generates tension to the fibers, which in combination with the fact that the material is molten while it is deposited, accumulation of material (droplets, blue circle in Fig.5) can be created. Moreover, irregularities in fiber deposition were observed in scaffolds higher than 1 mm [39]. It was hypothesized that the already fabricated scaffold was able to provoke electrical isolation.

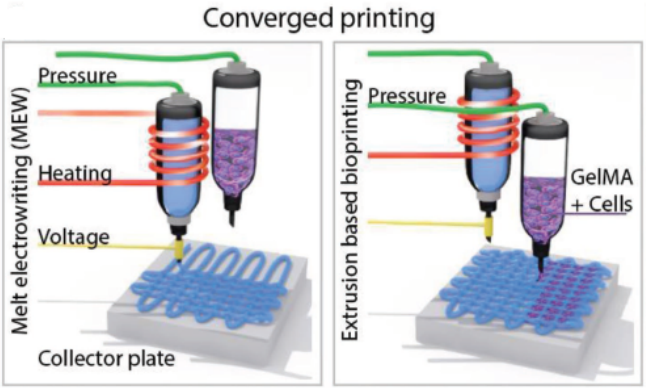


Fig. 4: Illustration of the one-step printing process. MEW, and extrusion-based bioprinting composing the converged printing. Adapted from [42]

Finally, in favor of cellular activities, the designed porosity should be examined. The minimum pore size that has been reported regarding the MEW-PCL[1] scaffolds is 150 µm [34]. In the case of smaller interfiber distances, the more intense generated repulsive forces led to the formation of unstable jet. A suggestion was to increase the pore interconnectivity by stacking the multiple layers in different orientations [33]. However, this could have an effect on the differentiation and the distribution of cells, and the mechanical properties.

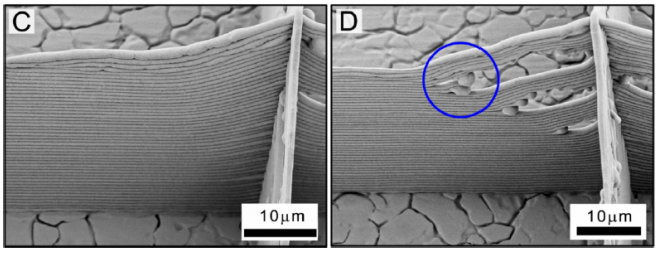


Fig. 5: Height difference close to the cross-sections of the MEW-deposited fibers (C), and structural gaps created by broken fibers (D). Adapted from [32]

1.4 Cartilage-bone interface

Successful integration of the chondral implant to the host articular cartilage, and the underlying bone is important to ensure an initial mechanical stability of the implant [43]. Compared to cartilage to cartilage and cartilage to bone interface, bone to bone interface has a faster, and more efficient integration [44]. Therefore, even in the case that the underlying bone is not affected directly (partial-thickness defects [45]), supporting the chondral implant by an osseous implant is beneficial for the initial mechanical stability of the first one.

The ECM of bone is composed of water, collagen (mainly type I), and carbonated hydroxyapatite (HA^2) [27] (70%), which constitutes an insoluble type of calcium phosphate [46]. These components provide the tissue with optimal strength and toughness, respectively. It is notable that they act synergistically. Hence, the accomplished strength and toughness of the tissue are greater than that of the components solely. Although the articular cartilage and the underlying bone are interconnected physically [27,47], the transition from one tissue to the other is not continuous regarding their mechanical properties [27].

1.5 Tissue engineering for bone regeneration

Compared to chondral implants, bone implants should be also non-toxic, and biocompatible. Inversely, their mechanical properties should be enhanced, and their porosity should be optimized to facilitate vascularization [48]. A biomaterial that aims to substitute the bone should be osteoconductive, osteoinductive, and able to provoke osteointegration. An osteoconductive material can stimulate bone formation on its surface by providing attachment sites for osteoblasts, and osteo-progenitor cells. Specifically, the native bone is directed toward the surface of the biomaterial. Inversely, an osteoinductive material is able to stimulate undifferentiated cells to develop into the bone-forming cell lineage. Osteointegration refers to the ability of the implant to promote robust bony tissue at the bone-implant interface. That is to say that no fibrous tissue is formed [49]. Materials such as metals, ceramics, and glasses fulfill the aforementioned properties [27].

Metallic materials (e.g., titanium, titanium alloys, and cobalt-chromium alloy) are commonly used in the fabrication of orthopedic implants, because of their high mechanical strength. However, metals are not suitable for bone regeneration. While, they do not degrade over time, corrosion and wear particles might occur. Moreover, phenomena such as stress shielding can be observed. Hence, the resorption of the surrounding native bone and an eventual loosening and/or failure of the implant can be detected [46].

The use of synthetic and natural polymers (e.g., PCL[1], collagen type I), and bioceramics (e.g., HA[2] and tricalcium phosphate (TCP) and bioactive glasses®) has been explored more extensively. Synthetic polymers have inferior mechanical properties, and osteoconductivity compared to the native bone. Although bioceramics satisfy those two criteria, they are susceptible to fractures under the application of substantial mechanical loads [27]. However, before their implantation, the minimally invasive surgical procedures that are applied require the implants to be deformable so as to be easily manipulated by the surgeons [50]. A combination of the two categories of material (synthetic polymers and bioceramics) could lead to a proper biomaterial for bone engineering [51]. This combination could recapitulate the composition of the native bone [46]. The brittle nature of bioceramics is attributed mainly to imperfections of their microstructure [52]. Therefore, the polymer can act as a filler of those imperfections and, hence, lead to enhanced roughness. Another approach is to use ceramics and bioactive glasses as blends on polymer materials [53]. Investigating this case, it was reported that bone healing was eased more extensively by the PCL[1]-TCP scaffold than the pure PCL[1] one [14]. Similar results were reported in the case of HA[2] and collagen composite scaffolds [46].

As a rule of thumb [54], extrusion-based techniques are applied to fabricate composite scaffolds. The most used approaches include the pneumatic-driven dispensing and the FDM. To enhance the osteinductive properties of the biomaterials, different biological agents have been incorporated. These are thermo-sensitive biomolecules, and, hence, ambient temperatures are required.

Recombinant human bone morphological protein-2 (RhBMP-2) has the greatest osteoinductive potency even though the results regarding the clinical safety are in dispute. Cases of heterotopic ossification, soft tissue edema, and cyst formation have been reported [48]. As a result, it is characterized as low cost-efficient [48,49]. In general, the effective delivery of all the biological agents (bone morphogenetic proteins (BMP), fibroblast growth factors, vascular endothelial growth factors, and platelet-derived growth factor (PDGF)) is dubious. The cells are highly sensitive to their concentration while the biological agents are unstable due to their short half-life [46]. However, the biological agents are of importance not to create a delayed union or a non-union [46]. To overcome these difficulties, advances on the available biomaterials have been developed. HB constitutes a prominent candidate in the category of synthetic osteoregenerative biomaterials. In an interesting study [50], HB for 3D-printing in ambient conditions was composed by combining HA[2], and PCL[1] or PLGA in the presence of a trisolvent mixture. Although the ceramic component was dominant (90 weight %), the material demonstrated elastic mechanical properties. This result is in accordance with the results of Li et al. [52]. Also, in the *in-vitro* evaluation, bone marrow stromal cells (BMSCs) were able to proliferate and differentiate toward the osteogenic lineage without the presence of any osteoinductive factor. Lastly, HB was assessed by an *in-vivo* model. No inflammation was reported, and osteointegration and vascularization were observed.

How the printing technique affects the nano-architecture of the deposited fibers constituted another research question of the study [50]. Particularly, room-temperature and hot-melt 3D-printed fibers were examined by a scanning electron microscope (SEM) (Fig.6). Apart from the surface characteristics, Fig.6 indicates that hot-melt fibers were brittle.

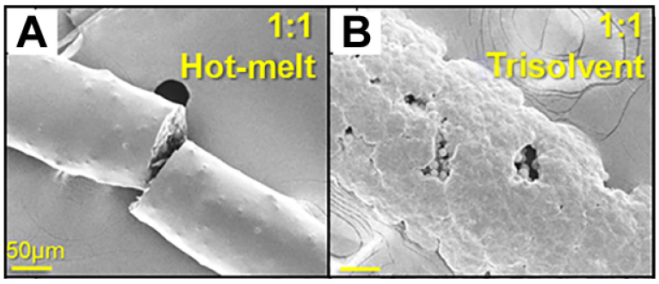


Fig. 6: Inversely to the extruded HB-fiber in ambient conditions (B), dense fibers without evident nano-architecture are observed in case of hot-melt HB-fibers (A). Adapted from [50]

1.6 Tissue engineering for osteochondral regeneration

The commonly followed approach to generate osteochondral implants is the fabrication of bilayered scaffolds. A bilayered scaffold should incorporate both a cartilaginous and an osseous compartment, which would be distinct but closely connected. Four different types of bilayered scaffolds have been reported in literature (Fig.7) [55].

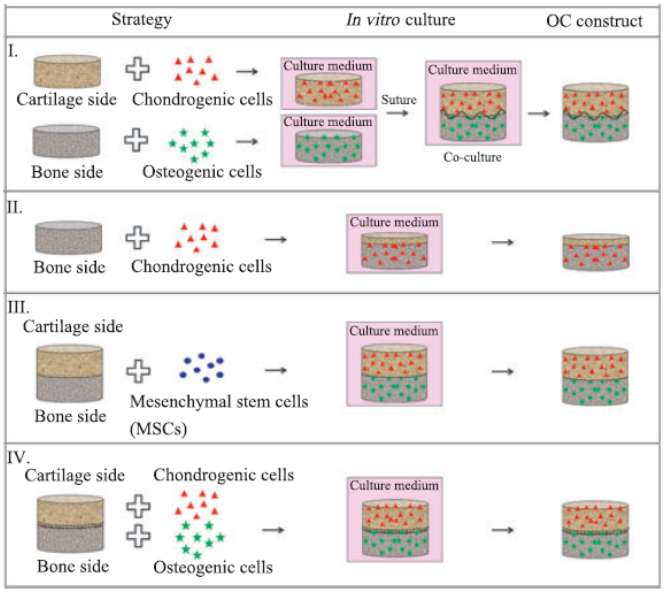


Fig. 7: The different types of bilayered scaffolds. I: The two-compartment scaffold for bone and cartilage regeneration, II: The scaffold-free approach for the cartilaginous compartment based on the osseous compartment, III: The single and homogeneous scaffolds, and IV: The single but heterogeneous scaffolds [55]

In the first case, a two compartment-scaffold is fabricated. Before the implantation takes place, it is converted into a single composite. This enables the use of chondrogenic and osteogenic cells, respectively, and their cultivation in cell-specific conditions [8]. Studies have shown that the seeded osteoblasts and chondrocytes produced distinct ECM in their compartment, and were able to integrate at the bone-cartilage interface [55]. However, in another study, it was reported that converting the two compartments into a single composite by suturing or gluing techniques, implies a potentially non-stable mechanical and biological interface [27]. For instance, even slight material-discontinuities can possibly harm the cell migration from the bone to the cartilage compartment [56]. Schaefer et al. [55] demonstrated that the culture period of the two compartments separately is critical for the

quality of the integration at the interface. It was concluded that the combination of a non-mature cartilaginous compartment and that of a mature osseous benefited their integration. Also, an *in-vivo* study explained that the loads of the knee joint constituted an additional factor that enhanced the interface integration [55].

In the second type, from the family of bilayered scaffolds, chondrocytes are seeded on the surface of an osseous compartment and cultured *in-vitro* to induce the formation of neocartilage tissue (Fig.7). Avoiding synthetic polymers as a cartilage equivalent could assist in achieving a non-acidic environment. However, studies have demonstrated that the interfacial shear strength of such scaffolds was lower compared to the native osteochondral one [55].

Subsequently, single and homogeneous scaffolds have been investigated. To stimulate the Mesenchymal Stromal Cells (MSCs) toward the chondrogenic and osteogenic lineage at the same time, specific coatings or blends have been used. For instance, Chen et al. [55] developed a bilayered scaffold by combining collagen as a cartilage and PLGA/collagen as a bone equivalent. The results confirmed that the two compartments were connected sufficiently. However, more sophisticated designs have been proposed, one of which suggested to split the osteochondral scaffold into four parts. A porous part was made from ceramic to imitate the bone compartment along with a dense part also made from ceramic to ensure that no blood vessels will penetrate the cartilaginous compartment. Also, this part was responsible for withstanding mainly shear forces. The third part was also ceramic and porous to achieve fixation between the osseous and the cartilaginous compartment. As the last part, a porous part made from synthetic polymer mimicked the cartilage.

Lastly, single but heterogeneous scaffolds have been developed. In that case, the two compartments are integrated yet distinct. Compared to the single and homogeneous scaffolds, in this case attention was paid to the layers of the interface. Therefore, different cell types could be seeded in the two compartments of the osteochondral scaffolds (Fig.7).

As in the case of chondral implants, the efficiency of the osteochondral implants is dependent on the specific internal architecture. The effect of the pore size of a bilayered PLGA scaffold on the regeneration of the osteochondral defects has been examined in an *in-vivo* model [44]. All the tested scaffolds were characterized by 85% of porosity. The optimal results were recorded with 100-200 µm and 300-450 µm in the cartilage and bone implant, respectively. As discussed by the authors, pore sizes smaller than 200 µm tend to facilitate chondrogenesis due to the hypoxic environment, whereas, pore size should not be less than 50-100 µm to facilitate cell infiltration and migration. Regarding the bony compartment, pore sizes ranging from 200 to 600 µm promote ostogenesis. As vascularization of the regenerated osseous tissue is required, the minimum pore size should be 300 µm. Also, it should be noted that the larger the pore size, the more deteriorated the mechanical properties would be. In a scaffold, the pores facilitate the diffusion of nutrients, but, at the same time, they constitute spots of stress peaks that finally weaken the mechanical strength [57].

1.7 Ex-vivo models for testing osteochondral implants

1.7.1 Available testing machines In the literature, to be able to describe the six degrees of freedom of the knee joint, a common system of coordinates has been established. Fig.8 summarizes the system of coordinates and the possible motions. Briefly, the system of coordinates is defined by the tibia's axis, the transverse axis of the collateral ligaments, and an arbitrary axis that is perpendicular to the other two axes. The complex motions of the knee joint can be condensed as a combination of translations and rotations. The first ones are notated as proximal-distal (d_{PD}), medial-lateral (d_{ML}), and anterior-posterior (d_{AP}). A respective notation is used regarding the rotations, internal-external rotation (Θ_{IE}), flexion-extension (Θ_{FE}), varus-valgus rotation (Θ_{VV}) [58].

The variability of knee motion sets experimental restrictions, since it is not straightforward to control the knee motion with high accuracy in the six degrees of freedom. Use of systems reproducing different degrees of freedom has been reported in the literature. Therefore, the results are not directly comparable. Currently, the robotic/universal force-moment sensor (robotic/UFS) testing system (Fig.9) is mostly used. The six degrees of freedom configuration allows for the application of multiple loading conditions. As a result, it is possible to collect data from the same specimen while it is exposed to different loading conditions. Hence, the effect of specimen to specimen variations on the raw data is limited, and the statistical power of the data is enhanced. Another advantage of the particular testing system is the ability to operate in two modes, allowing the researcher to choose the optimal mode according to the particular case study. The two modes are the force and the position control mode. In the first case, a specific load is applied, and the resulting translations and rotations are recorded. Inversely, the position control

mode demands the knee joint to be subjected under a predefined motion path. Recording the generated forces and momentums in all directions, it is possible to figure out the magnitude and also the direction of the applied load [58]. The measuring accuracy of this testing system is 0.02 mm and 0.02° for position and orientation, and 0.2 N and 0.01 N m for forces and momemtums in the force and the position mode, respectively.

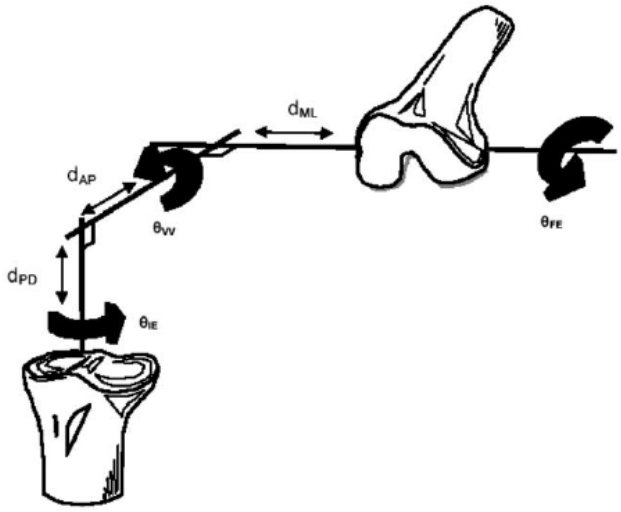


Fig. 8: Schematic representation of the knee joint motions and the established anatomical axes [58]

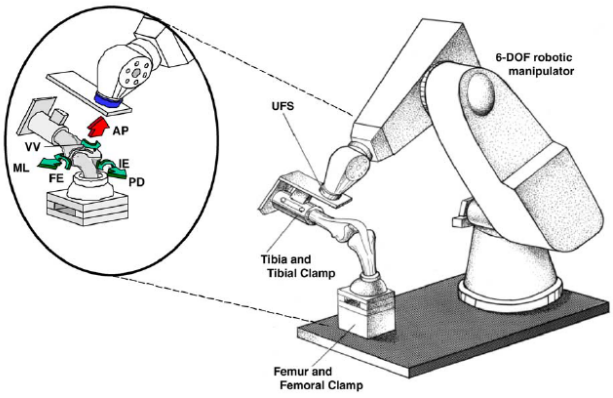


Fig. 9: The robotic six-degrees of freedom mechanical testing system as illustrated by [58]

1.7.2 Comparative biomechanical analysis of human and animal knee models Before proceeding to clinical trials, both the biological and the mechanical features of an osteochondral implant have to be examined. Besides satisfying specific requirements regarding biocompatibility and chemical stimuli, the implants should be able to be mechanically stable under the application of forces that are generated *in-vivo*. Sittinger [59], pointed out that positive long-term results of an implantation are dependent on the insurance of sufficient joint surface congruity. Therefore, the mechanical stability of grafts is of high importance. To perform a biomechanical analysis, bio-reactors, *ex-vivo* and *in-vivo* models are commonly used. However, as the first two systems are not capable to

induce complex immune responses, in order to overcome these limitations, *in-vivo* studies should be performed as a final testing method before proceeding to clinical trials. The disadvantages of the *in-vivo* testing systems are their time-consuming nature, and the high cost of breeding and housing the animals.

Therefore, the focus of the following sections of the introductory chapter will be to investigate the *ex-vivo* animal models used to examine the mechanical stability of osteochondral implants. However, the selection of the more suitable *ex-vivo* model is of great importance. The results of each *ex-vivo* model should be evaluated and correctly translated to the human biomechanics. Because of the variability in the physiology and the anatomy of joints within different species, a safe conclusion could be made by executing a comparative study. Based on extensive work [60], findings regarding the intra-articular knee anatomy of different models are summarized in Table 1 and Table 2.

Table 1: Grading of anatomical similarity of different animal models with human knee. (+) good, (∘) adequate, (-) no similarity in absolute, normalized sizes, and anatomical features with the human one. Adapted from [60]

	ACL	PCL^2	Medial Meniscus	Lateral Meniscus	Intercondylar Notch	Overall Score
Bovine	+	∘	-	-	∘	-
Caprine	+	-	∘	+	-	∘
Porcine	∘	-	-	∘	-	-
Ovine	+	-	∘	∘	∘	∘
Canine	-	-	-	-	∘	-
Lapine	-	-	-	-	∘	-

Table 2: Measurements of the range of motion in different knee models. Adapted from [60]

	Degrees of extension	Degrees of flexion
Human	2.5±2.9	137.5±9.6
Sheep	40±5	146.7±2.9
Goat	45±9.1	145.5±8.7
Dog	34±4.2	160±3.5
Cow	35±5.8	145±7.1
Pig	42±4.5	144±5.5
Rabbit	22±2.7	161±2.2

Briefly, the bovine and the ovine anterior cruciate ligament (ACL) presented both comparable absolute and normalized size. The normalization was based on the tibial plateau width. As far as the anatomical sites are concerned, the caprine specimens had similar tibial insertion sites to the human specimens, although their length was significantly smaller. Continuing to the posterior cruciate ligament (PCL^2), only the bovine model satisfied the human analogous in all the terms. Concerning the meniscus, discrepancies were observed among the medial and lateral one. The medial meniscus of the ovine and the caprine model was more closely related to the human one in terms of the absolute and normalized size. Inversely, the lateral meniscus was comparable in size to the ovine, the caprine, and the porcine ones. However, the tibial insertion sites in the caprine specimens had the best match with the human [60]. These findings indicate that the caprine model is the optimal selection for case studies in that the role of the meniscus as an entity is crucial. Finally, the caprine and the porcine models were the most differing to the human intercondylar notch. Based on these results, it is noticeable that the selection of each model is application-specific, since different pathologies of the knee joint are optimally examined by different *ex-vivo* models. Based on the overall score of the different animal models in Table 1, the caprine and the ovine models

seem to be the optimal selections to replicate the overall knee biomechanics. Fig.10 represents the gross differences of the human and the two aforementioned animal models.

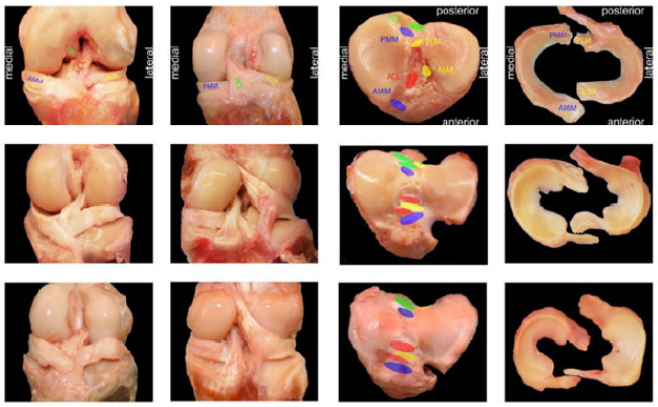


Fig. 10: Knee joint physiology and anatomy of the human (first row), the ovine (second row), and the caprine (third row) model. Adapted from [60]

Concerning the caprine model, anatomical discrepancies were reported in the articular geometry compared to the human based on computed tomography (CT) and magnetic resonance imaging (MRI) scans [61]. The goat menisci were thicker and covered proportionally to a greater extent the tibial articular surface. Fig.11 indicates the anatomical differences of the two knee joints. As it can be seen, the tibia articular surface presents higher convexity in the sagittal direction. It is established that the range of flexion is mainly dependent on the specific features of the articulation's geometry and the insertion sites of the knee ligaments. It has been measured that, during walking and trotting, the knee of a goat is flexed in the range of 40-80° [62]. Inversely, during walking, the human knee is subjected to flexion that ranges between 0° and 40-60° [63]. The ACL presents three bundles (anteromedial, intermediate and posterolateral) in both models [64,65,66]. The anteromedial bundle constitutes the main restrictive factor at 90° of flexion, while the posterolateral one is dominant in the range of 0-30° of flexion [67]. The translations and the rotations of the caprine stifle were reported to be less restrictive by the intermediate bundle [68]. Although the range of knee motion is different in the caprine and the human model, both of them show a maximum of approximately 140° from the less flexed position [62,63].

Regarding the characteristics of the articular cartilage, it was pointed out that, while the elastic Young's modulus of goats was higher (averaged on 0.19 MPa), the thickness of articular cartilage was constantly lower (averaged on 1.06 mm) [61]. However, the trochlear and the tibial plateau presented the thinnest cartilage in the caprine and the human model, respectively.

Patil et al. [61] tested the human and caprine specimens from 0° up to 30° and from 50° to 70° of flexion, respectively. This choice was made based on gait analysis data. Particularly, the stance phase of walking was examined. It was noted that, normalized to the body weight (BW), loading conditions in the human and caprine knee are similar, 2.2 and 2.1 × BW, respectively.

Table 1 indicates that the ovine model constitutes an alternative to the caprine model. The *in-vivo* kinematics of female Suffolk cross-sheep were investigated while walking on a flat and an inclined treadmill, and while trotting [69]. It was measured that the flexion of the stifle joint ranged from 43.1° to 77°. Compared to the caprine model, the ovine one has thinner articular cartilage. Hence, the caprine model is closer to the thickness-values of the human articular cartilage [70]. In regard to the meniscus of the ovine model, it was reported that both the medial and the lateral meniscus have comparable thickness to that of human [71].

The Osterhoff group[72] compared the gross anatomy of the knee between the ovine and human species. The results indicated a trend of the epicondylar width, the width of both the medial and lateral condyle, the tibia's dimensions to be three times smaller in the ovine model compared to the human one. These results are in accordance

with the fact that the femural articular cartilage surface is not continuous in the ovine model. A main difference was also observed in the shape of the tibial plateau. Compared to the oval shape in human, sheep have a triangular shape. Also, in human, the trochlear width and the intercondylar notch were measured to be bigger. Therefore, the patella in sheep needs to be more elongated to anchor to the trochlea groove. However, the thickness of patella is barely the same as that of human. Hence, the patellofemoral articular surface is subjected to greater shear stresses compared to the tibio-femoral joint in ovine. The particular condition is contradictory to the ratio of shear stresses in the human knee.

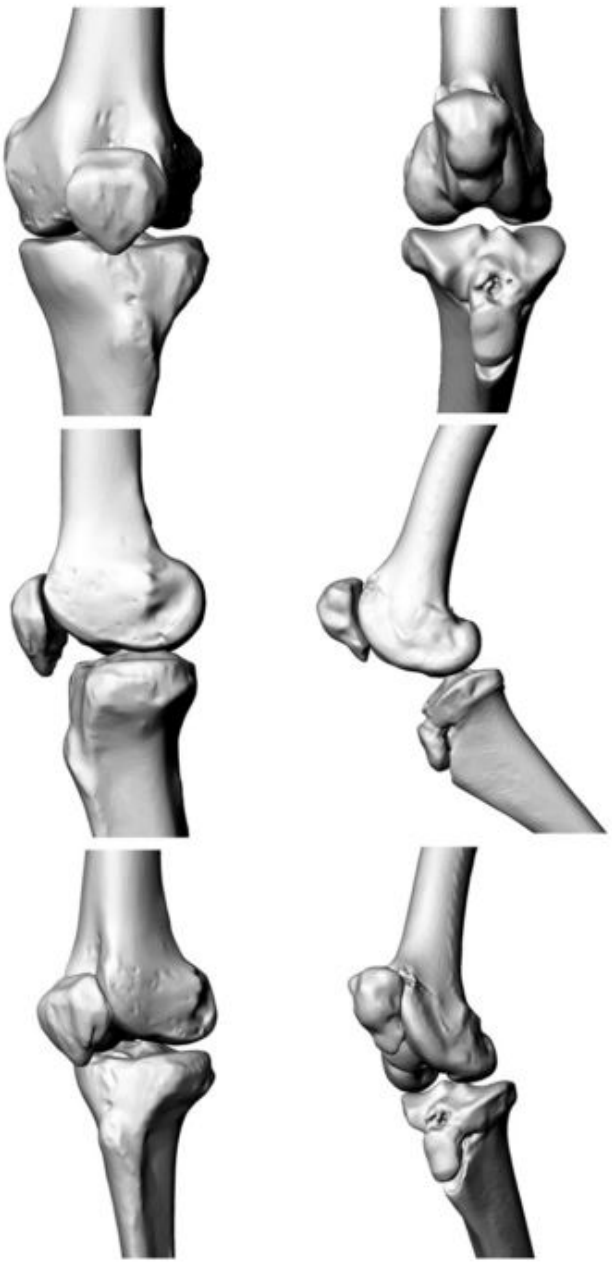


Fig. 11: Geometry of human (on the left) and caprine (on the right) knee. Top: anterior view, middle: lateral view, bottom: oblique view [61]

The geometry of articulation is critical to determine the range of knee motion in every species. Table 2 indicates that the ovine stifle can be flexed in the same range as the caprine one. The absolute values range from 40° to 146.7°. As it has been reported [73], the cranial cruciate ligament (CraCL) of the ovine stifle is consisted of the craniomedial bundle (CraMB) and the caudolateral bundle (CaudLB). Their function resembles the function of the anteromedial and the posterolateral bundles of the human ACL, respectively. In the same study, it was demonstrated that the CraCL is a main restrictive ligament for the external rotation of the stifle. This is in disagreement with the human model.

Regarding the applied forces, the knee contact force was mounted to 2.25 × BW [74]. This measurement was extracted while applying the inverse dynamics analysis on *in-vivo* data of sheep during gait. The authors compared the results to those of humans while walking. Using similar musculoskeletal models, forces ranging from 2.8 to 3.8 × BW have been reported. The observed difference might be attributed to the quadrupedal nature of the sheep.

1.8 Conclusions from previous studies

The aim of the introductory chapter was firstly to determine the used biomaterials in bioprinting for osteochondral biofabrication and the compatible *ex-vivo* techniques, and, secondly to evaluate different animal *ex-vivo* models as equivalent of the human biomechanics. The following conclusions can be drawn. Progress in the frequently used biomaterials and bioprinting techniques has been recorded for cartilage and bone regeneration, respectively. The optimal osteochondral scaffold is not yet developed. To develop an osteochondral scaffold using bioprinting, the convergence of different biofabrication techniques is required. Following this, the development of the six-degrees of freedom mechanical testing systems allows applying complex loading conditions with high precision. Despite the latest advancements in testing systems, the selection of the most suitable animal *ex-vivo* model is critical to translate the results to human biomechanics. The comparative analysis of different animal models indicated that the caprine and the ovine models constitute the optimal ones to emulate the overall knee biomechanics. However, complex immune responses cannot be simulated. Therefore, *in-vivo* studies should be the following point to be investigated. Finally, clinical trials constitute the ultimate testing system, which unavoidably cannot be replaced by any means.

1.9 Thesis objective and research aims

It can be concluded from the previous sections that there is the need to fabricate osteochondral implants even in the case of partial-thickness defects. Yet, anatomically shaped osteochondral implants cannot be developed. The limitation arises from the different materials and bioprinting techniques used to fabricate the articular cartilage-, and bone-equivalent, respectively. For the current work, the thesis objective was to fabricate large bone-implants for osteochondral regeneration. To achieve this, the following research aims were set: (1) converge MEW and extrusion-based techniques; (2) introduce biologically and mechanically functional large osteochondral implants; (3) determine the stiffness of osseous implants in respect to the proposed design and the *in vitro* pre-culture conditions; (4) evaluate the correlation between the size and confinement of osseous implants to their mechanical stability using an *ex-vivo* testing system; (5) assess the extent of fusion of the compartments of a single but heterogeneous osteochondral implant.

Materials and Methods

2.1 Convergence of MEW and extrusion-based techniques

The integration of an osseous compartment and a cartilaginous one, fabricated by extrusion-based 3D printing techniques, and extrusion-based 3D printing techniques and MEW, respectively, could lead to the development of a single but heterogeneous osteochondral implant. To generate the printing path of the MEW print-head based on the geometry of the osseous compartment a code written in Python was developed. Fig.12 indicates the main processes of the Python-code. The specific code creates a MEW-fabricated box-architecture on top of an osseous implant of a human condyle (Fig.13). The inter-fiber spacing was selected at 0.2 mm. The reasoning is that pore sizes between 0.1 and 0.2 mm facilitate chondrogenesis [44]. However, inter-fiber spacing smaller than 0.15 mm has been reported to result in unstable jet due to the intense generated repulsive forces [34]. Also, the printing velocity was set at 5 mm/ sec.

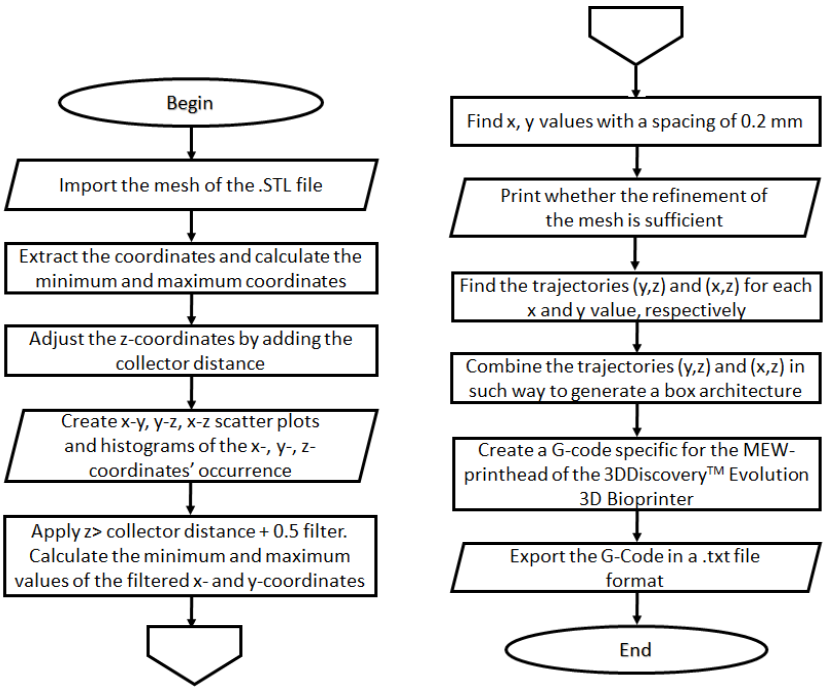


Fig. 12: The flowchart of the developed Python-code

2.2 Anatomically shaped implants

To acquire the precise anatomy of the sheep stifle, μ-CT data were acquired at the Medical Engineering Research Facility (MERF) of Queensland University of Technology.

The reconstructed CT models were segmented by hand while using as a threshold the default bone value of the software (Slic3r 4.10.2). Three segments were chosen, namely the tibia, the femur, and the patella. At the same time, a joint smoothing value of 0.3 was selected. Each segment of the stifle-joint was exported into Standard Tessellation Language (STL) format. The STL files were then imported on MeshLab (2016.12) to smooth the mesh by a three-step Laplacian smooth process.

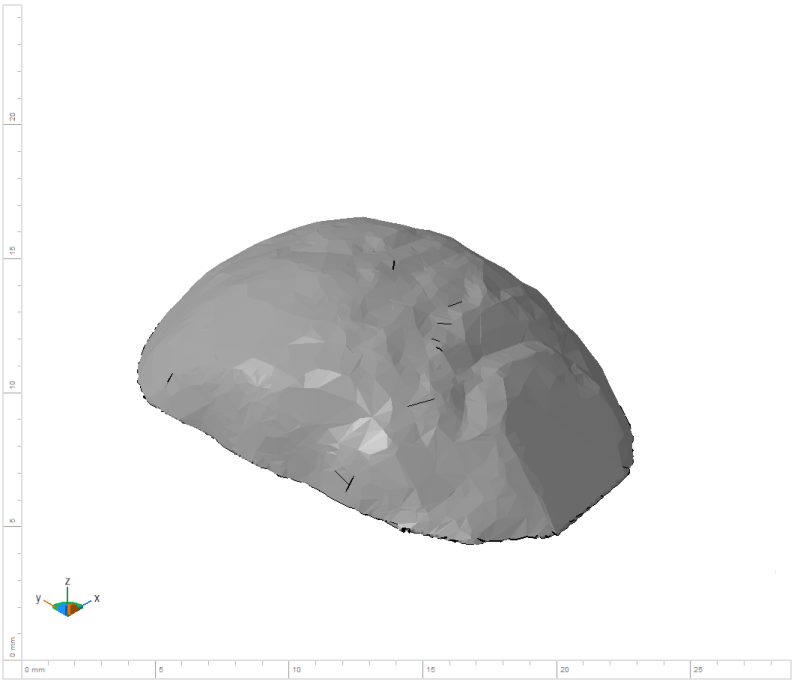
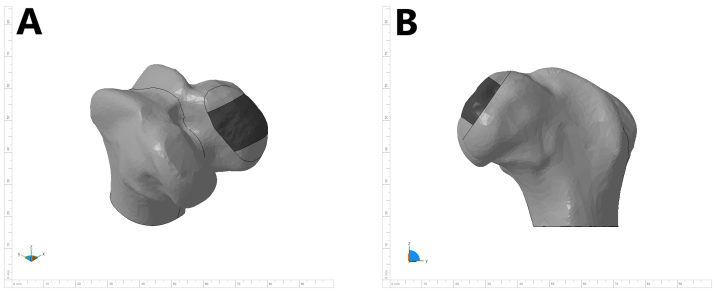


Fig. 13: Illustration of the .STL file of a human condyle

2.3 Introducing large osteochondral defects

To identify whether there is a critical size of a bone-defect that can be replaced by an implant without harming the integrity of the knee-joint, four different types of defects were created. In the first three defects, the width of the defect was considered as a parameter of interest, while in the fourth defect the confinement of the implant from the surrounding material was evaluated as a mean of stability. Particularly, the defects were created concentrically on the medial condyle of the femur by forming a 55° inclination with the horizontal plane (Autodesk Netfabb Premium 2019, San Rafael, United States). Fig.13 illustrates the isometric, and the side view of both the defects (grey) and the implants (black). Each defect and implant was exported in the format of an STL file.



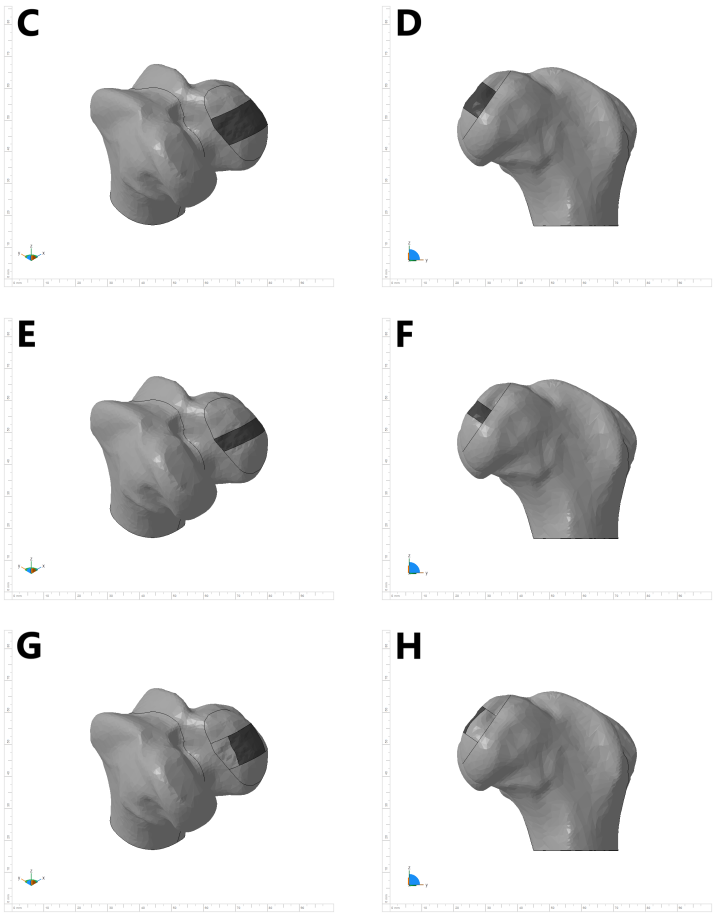


Fig. 13: Four types of defects and the corresponding implants. A: Isometric view of defect I and implant I (17.87 × 15.05 × 6.22 mm), B: Side view of defect I and implant I (17.87 × 15.05 × 6.22 mm), C: Isometric view of defect II and implant II (19.15 × 9.99 × 6 mm), D: Side view of defect II and implant II (19.15 × 9.99 × 6 mm), E: Isometric view of defect III and implant III (19.12 × 5 × 5.95 mm), F: Side view of defect III and implant III (19.12 × 5 × 5.95 mm), G: Isometric view of defect IV and implant IV (10 × 10 × 6 mm), H: Side view of defect IV and implant IV (10 × 10 × 6 mm), (length×width×height)

2.4 Implants fabrication via FDM

Each implant-STL file was imported on BioCAM^{TM} (regenHU Ltd, Villaz-Saint-Pierre, Switzerland) software. The design of the implant was based on the principle of limiting the cellular and vascular penetration from the osseous compartment to the cartilaginous compartment and the knee-joint space. Four outer loops were designed in the periphery of the osseous implant to ensure that no cells and vessels penetrated the knee-joint space (Fig.14-A). As Fig.14-B illustrates, this approach does not refrain the penetration to the cartilaginous compartment. For that reason, solid horizontal layers at the top/bottom were also chosen (Fig.14-C, D). To generate an implant with a closed surface, layers of Fig.14-B and Fig.14-D were combined in an appropriate way.

To print the PCL[1] implants via FDM, a 3D-bioprinter (3DDiscovery Evolution, regenHU Ltd, Villaz-Saint-Pierre, Switzerland) was utilized in ambient conditions. PCL[1] (PURASORB PC 12, Corbion, Gorinchem, The Netherlands) was loaded in the heating chamber in pellet form. The cartridge temperature was set at 90 °C, while the temperature of the nozzle was lower by 10 °C. The extrusion of the melted PCL[1] was controlled by a screw-system at a constant feed rate of 2 revs/minute. Using a nozzle of 27 Gauge (regenHU Ltd, Villaz-Saint-Pierre, Switzerland), to achieve proper deposition, the printing speed was set at 2 mm/ sec and the pressure at 0.140 MPa. Particularly, a 0-90° lay-down pattern was followed. The infill density was set at 20%, the overlapping perimeter

at 15% and the layer height at 0.2 mm. After fabricating, the dimensions of the generated implants were measured to assess the dimension fidelity of the printing process. To quantify, the following mathematical formula was used:

$$\text{Overall dimension fidelity } (\%) = \left(1 - \frac{\text{accuracy in x-direction} + \text{accuracy in y-direction} + \text{accuracy in z-direction}}{3}\right) * 100 \quad (1)$$

while the accuracy in each direction was calculated by the formula described in Equation 2.

$$\text{Accuracy in each direction } (\%) = \left(\frac{\text{Optimal dimension} - \text{Real dimension}}{\text{Optimal dimension}}\right) * 100 \quad (2)$$

2.5 Composite of HB ink

To form the HB ink, PCL[1] (28% w/v) in pellet form, micro-scale magnesium-phosphate powder (Magnesium phosphate hydrate $\geqslant$ 98% (ignited basis), Sigma-Aldrich, Steinheim am Albuch, Germany) (33% w/v), and a three-solvent were thoroughly mixed in a rolling plate for two to three days. The three-solvent was composed of dichloromethane (Honeywell Riedel-de-Han^{TM}, Fisher Scientific, Bleiswijk, The Netherlands), 2-butoxyathanol (Ethylene glycol monobutyl ether for synthesis, Merck Millipore, Amsterdam-Zuidoost, The Netherlands), and dibutyl phthalate (Dibutyl phthalate 99%, Sigma-Aldrich, Steinheim am Albuch, Germany) in a ratio of 10:2:1. Prior to printing, the HB ink was occasionally stirred by hand in a chemical hood to achieve the evaporation of excess dichloromethane.

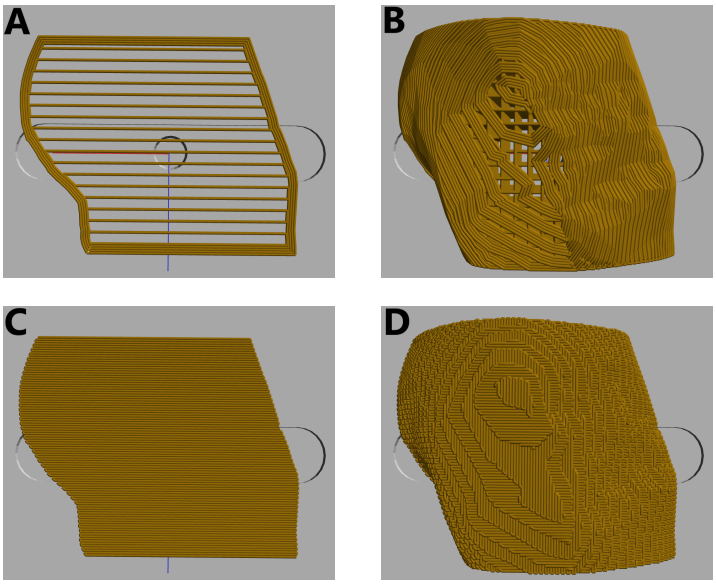


Fig. 14: Combined designs to generate an osseous compartment with four loops in the periphery and closed top layers. A: Top view of the printing path of the four-looped design, B: Top view of the whole construct of the four-looped design, C: Top view of the printing path of the solid design, D: Top view of the whole construct of the solid design

2.6 Implants fabrication via pneumatic-driven dispensing

The same strategy in terms of design was also followed in the case of HB-implants as in Section 2.4 (Fig.14). However, as this particular design does not facilitate bone integration in the native bone-implant interface. An additional design was, therefore, also conceptualized and fabricated. Particularly, one loop of material was designed in the periphery of the implant, but the sides of the native-bone interface were manually deleted (Fig.15-B). This

modification resulted, however, in decreasing the dimensions of the printed implants. Therefore, the two designs of Fig.15 (B, C) were combined. As illustrated in Fig.16, the optimal combination was achieved using the one-loop design and the no-loop one, scaled by 100% and 97%, respectively. At the same time, a few of the top layers were replaced by the solid design (Fig.14-C, D) to ensure the closed osseous-cartilaginous interface.

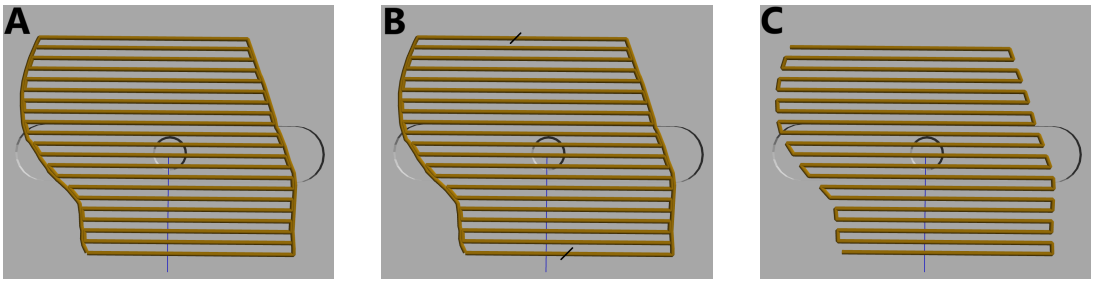


Fig. 15: Creating a porous implant at the implant-native bone interface while maintaining the outer periphery loop at the side of the knee joint space. A: Top view of the printing path of the one-loop design, B: The black cross-lines indicate the deleted parts of the periphery loop, C: Top view of the printing path of the no-loop design

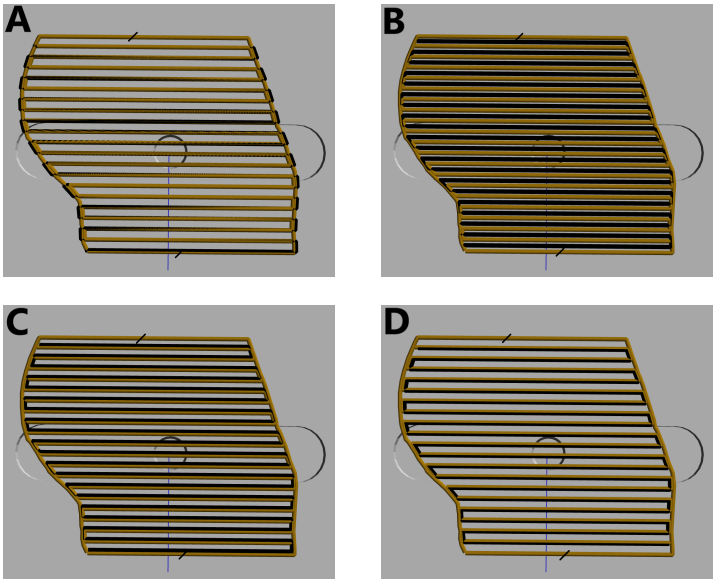


Fig. 16: Converged printing path. A: The one-loop design combined with the no-loop one, scaled by 100%, B: The one-loop design combined with the no-loop one, scaled by 100% and 98% respectively, C: The one-loop design combined with the no-loop one, scaled by 100% and 97% respectively, D: The one-loop design combined with the no-loop one, scaled by 100% and 96% respectively

Because of the viscosity inconsistency of the HB ink, of high interest was to preserve the porosity and the fiber diameter of each implant. Hence, prior to the actual implant fabrication, a few layers were printed to evaluate the pore size and the fiber diameter under a stereo-microscope (Olympus SZ61, Olympus, Tokyo, Japan). The magnification was set at 0.8×. The optimal fiber diameter was set at 300 µm, while the pore size was allowed to range from 400 to 450 µm. The HB-implants were printed with a 3D-bioprinter (3DDiscovery Evolution, regenHU

Ltd, Villaz-Saint-Pierre, Switzerland) in ambient conditions. On each occasion, a 5 mL cartridge was loaded with HB ink. The implant design was based on an alternating 0-90° lay-down pattern using a conical shaped 22 Gauge nozzle (Precision Tips Engineered Fluid Dispensing, Nordson EFD, Maastricht, The Netherlands). The print-head velocity was set at 5 mm/min, while the pressure ranged from 0.060 to 0.210 MPa. The infill density of each layer was set at 35%, the overlapping perimeter at 15%, and the layer height at 0.2 mm. After printing, the dimensions of the generated implants were measured to assess the dimension fidelity of the printed implants. The mathematical formulae described in Equations 1 and 2 were used, respectively. To carefully remove the solvents and sterilize the implants, they were washed in 70% ethanol for six hours and subsequently in Milli-Q water for twenty-four hours.

2.7 Scaffold fabrication for mechanical testing bulk materials: PCL[1]

To measure the Young's modulus elasticity of PCL[1] under compression, scaffolds were cast to measure the bulk properties. The casting-molds were made of silicone and their dimensions set at ⌀ 10mm × 20 mm. PCL[1] was placed in the form of pellets into the casting-molds and heated for 20 minutes at 90 °C. Additional pellets were included and heated for another 20 minutes to fill the volume of the casting-molds. sTo achieve a perfectly flat surface of the cast-scaffolds, they were post-processed by trimming their surface using a sandpaper. The resulting dimensions and weight of each sample were measured.

2.8 Scaffold fabrication for mechanical testing of materials: HB

Three different types of scaffolds were fabricated to investigate the effect of the loop design and the closed top layer on the stiffness of the HB implants. Also, the possible deterioration of the stiffness of the implants after a culture period of 28 days in chondrogenic differentiation medium was examined. The chondrogenic differentiation medium was made from Dulbecco's Modified Eagle Medium (Thermo Fisher Scientific, Bleiswijk, The Netherlands), Corning^{TM} ITS Premix Universal Culture Supplement (Fisher Scientific, Bleiswijk, The Netherlands), ASAP^{TM} AGAR (Marcy-l'Etoile, France), Penicillin-Streptomycin (Thermo Fisher Scientific, Bleiswijk, The Netherlands), Dexamethasone Fluirescein (Thermo Fisher Scientific, Bleiswijk, The Netherlands), and Transforming growth factor-β1 (TGFβ1) (Thermo Fisher Scientific, Bleiswijk, The Netherlands). The culture conditions were set at 37 °C and at 5% of carbon dioxide (CO_2) (Panasonic MCO-170, PHC Europe B.V, Etten-Leur, The Netherlands). Since any cell type was included, no medium change was carried out.

The optimal dimensions of the tested cylindrical scaffolds were ⌀ 8mm × 8 mm. However, the actual dimensions of the generated scaffolds were measured after printing. To carefully remove the solvents and sterilize the scaffolds, they were washed in 70% ethanol for two hours and subsequently in Milli-Q water for eight hours. The printing protocol, in this case, was the same as that in the case of HB-implants. However, to be able to print these scaffolds, a decrease in the printing speed was required. The printing speed was set at 3 mm/min, while the pressure ranged from 0.065 to 0.095 MPa.

Moreover, cast scaffolds were created to quantify the bulk properties of HB. The casts were made of PLA (Signal White, MakerPoint, Utrecht, The Netherlands) using a 3D printer (Ultimaker 3, Ultimaker, Utrecht, The Netherlands). Their dimensions were set at ⌀ 10mm × 20 mm. The material was cast for two days. Sterilization and removing solvents were performed as described in Section 2.6. The same trimming process was performed as described in Section 2.7.

To acquire an insight as to whether the casting-process resulted in a homogeneous dispersion of the material in the casting-molds, μ-CT (Quantum FX, Caliper Life Science, Hoofddorp, The Netherlands) data were acquired prior to the compression test. The used set-up was as following: the voltage at 90 kV, the current at 200 µA, the field of view at 24 mm, and the scan time at 4.5 min.

2.9 Mechanical testing of scaffolds

To assess the stiffness of the scaffolds under compression, unconfined uniaxial compression (Lloyd Instruments Ltd LR 5K, Lloyd Instruments Ltd, Bognor Regis, United Kingdom) was performed. A load cell of 5 kN was used and a pre-load of 0.1 N was applied. The fabricated samples were compressed to a 2.5 mm deformation (31.25% of the height), while the cast ones to 8 mm ($\approx$ 40% of their height). The rate of deformation was set at 1 mm/min. In each group, at least six scaffolds were tested, *i.e.* scaffolds with one closed top layer and periphery loop ("enclosed"),

cultured scaffolds with one closed top layer and periphery loop ("enclosed-28"), scaffolds without a closed top layer and with periphery loop ("encircled"), scaffolds with one closed top layer and without periphery loop ("open"), HB-cast scaffolds (HB-Cast), and PCL^1-cast scaffolds (PCL^1-Cast).

From the acquired data (recorded force and displacement), the stress-strain curves were extracted. In the case of non-cast samples, the average diameter and height were considered to perform the required calculations instead of the ideal values. The stress was defined as the applied force divided by the unloaded average cross-sectional area ($\sigma = F/A$). Although the minimum cross-sectional area of each sample should have been used, the deviation of the average diameter allowed to consider the average diameter for the calculations of all the samples. To calculate the strain values, the deformation at each time point divided by the average height of the scaffolds was calculated ($\varepsilon = \Delta L/L$). Inversely, in the case of cast-scaffolds the dimensions of each sample were considered to perform the aforementioned calculations. For each scaffold, the apparent Young's modulus elasticity was calculated based on the slope of the stress-strain curve. For this reason, a linear function was fitted in the elastic area of the data. Any toe region was neglected.

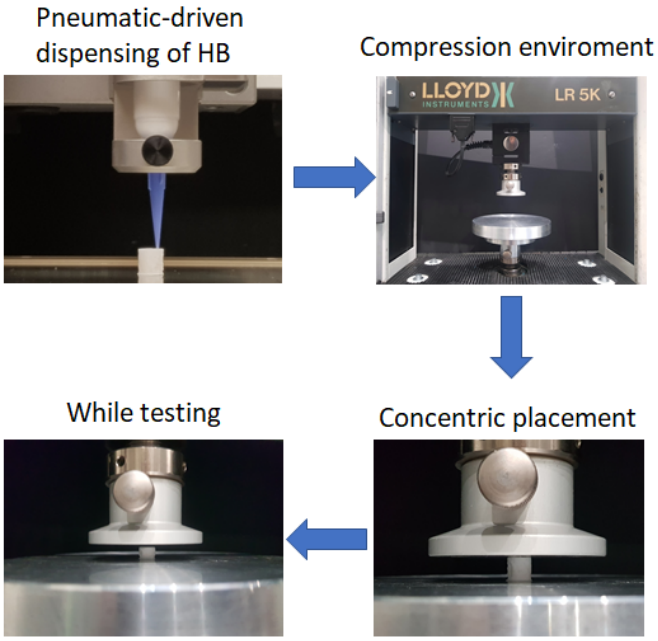


Fig. 17: The workflow from fabricating the HB-scaffolds to their compression

2.10 Digital Light Processed *ex-vivo* model

To fabricate an equivalent *ex-vivo* model, digital light processed (DLP) 3D-printing technique (EnvisionTEC Perfactory 4 DDP M, EnvisionTEC GmbH, Gladbeck, Germany) was used. A liquid photopolymer (R5, EnvisionTEC GmbH, Gladbeck, Germany) was used in combination with a 60 mm lens. The resolution of this printing set-up was 0.5 mm and the lamp power was set at 550 mW/dm^2. The tibia, the patella, the intact femur, and the four different types of defective femurs were fabricated. The produced supports were removed manually after printing. Following this, the fabricated designs were placed in a 70% ethanol-bath for eight hours to remove the uncured resin.

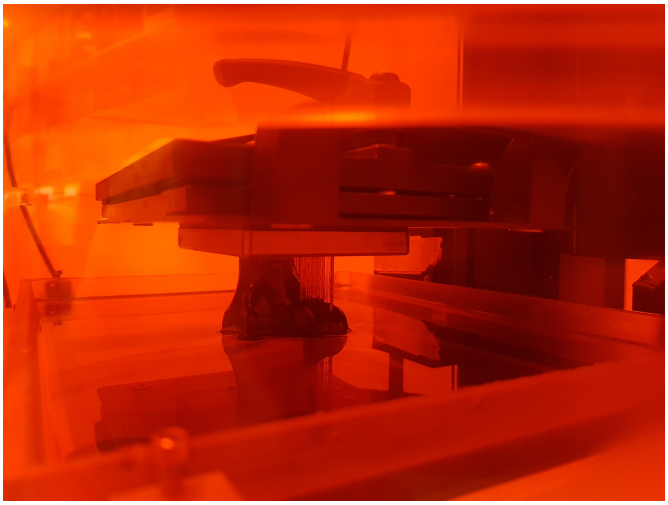


Fig. 18: Fabricating an anatomically-shaped femur using DLP technique

2.11 Testing PCL[1]-implants on the DLP *ex-vivo* model

To execute the specific testing, the DLP-fabricated tibia, and the different femur types (Defect I, Defect II, Defect III, Defect IV) were fixed at the top and bottom compression plates, respectively (Fig.19). The universal, static testing system (Instron 5967, Instron, Norwood, United States) was operated by Roderick Verberne. Particularly, a load cell of 30kN was used. The rate of the applied force was set at 400 N/ sec, while the maximum recorded force was 2000 N. The implants were introduced to the points of the defect without any means of fixation. In total, each implant underwent six cycles of loading, and unloading in three different degrees of flexion (50, 55, and 60 °). These degrees of flexion represent the range of flexion from the midstance to the midswing phase of the gait cycle of an ovine stifle while walking [74]. The contact area at the different degrees of flexion was calculated using a colored dye.

From the acquired data (recorded force and displacement), the force-displacement curves were created. Hence, it was possible to evaluate whether the type of the implant affects the joint congruity by calculating the energy ratios in each testing. Also, the contact stress at the maximum force was calculated. It was defined as the maximum applied force divided by the contact area. Afterward the testing of the implants on the DLP *ex-vivo* model, the height of each implant was measured.

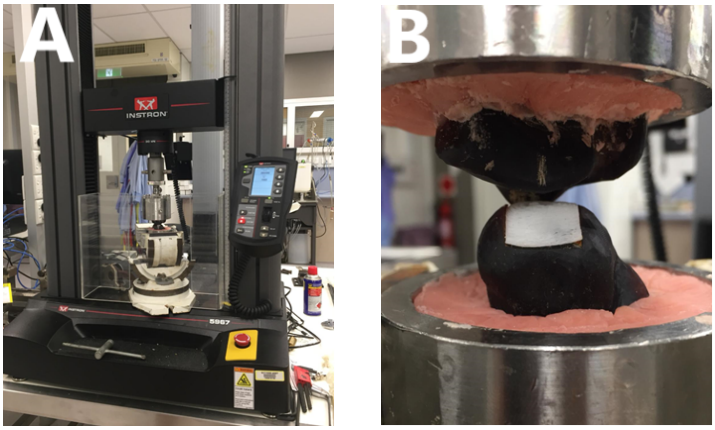


Fig. 19: A: Instron 5967, the universal, static testing system used in the case of the DLP *ex-vivo* model, B: Fixation of the DLP-model on the compression plates

2.12 Fusion of PCL[1]-, HB-, and PCL[1]- and HB-fibers

The fusion of PCL[1] to PCL[1]-, and HB to HB-fibers was evaluated by examining slices of fabricated implants by SEM (Phenom Pro Desktop SEM, ThermoFisher Scientific, Pittsburgh, PA, USA). To investigate the fusion of PCL[1] and HB-fibers, a MEW-fabricated box architecture was deposited on top of the HB-fabricated shapes of Fig.20. The dimensions of the rectangles were set at 19×15×2 mm (Rectangle A) and 19×10×2 mm (Rectangle B) (length×width×height), resembling the length and the width of implants I and II. The selection of two different dimensions was performed to evaluate the fusion of HB-, and PCL[1]-fibers, as a function of the elapsed printing time. The fabrication time per layer is dependent on the printing velocity, the fiber diameter, the inter-fiber spacing, and the total surface area that needs to be printed [42]. In the particular case study, only the total surface area was considered as a parameter. The HB-rectangles were fabricated by combining the one-loop design (Fig.15-A) of the HB implants by replacing the last layer by the solid design (Fig.14-C) . An alternating 0-90° lay-down pattern using a 22 Gauge nozzle was selected. The infill density of each layer, the overlapping perimeter, and the layer height were similar as previously described (Section 2.6). Regarding the MEW-deposited PCL[1]-fibers, an inter-fiber spacing of 0.4 mm was selected. A 3D-bioprinter (3DDiscovery Evolution, regenHU Ltd, Villaz-Saint-Pierre, Switzerland) was used with a conductive 24 Gauge nozzle. The printing parameters of both techniques are summarized in Table 3.

Regarding the SEM analysis, no prior washing steps were followed. The samples were mounted on specific stubs and, to avoid artifacts such as charge buildup, the surface of the samples was sputtered by a 4nm-thick layer of gold under vacuum pressure (≈ 0.1 mbar), using a machine (Q150R S, Quorum Technologies, Judges House, United Kingdom). The magnification in SEM ranged from 225× to 4900×, while the applied voltage was set at 5-10 kV.

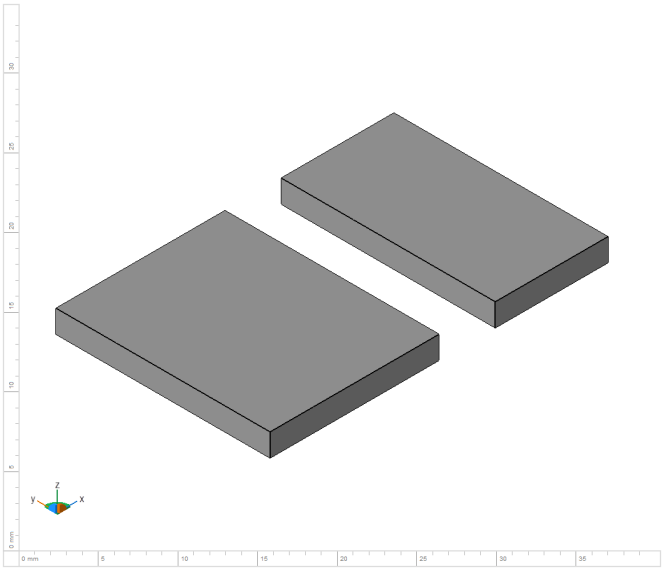


Fig. 20: The design of the two HB-rectangles fabricated via pneumatic-driven dispensing to investigate the fusion of MEW-deposited PCL[1]-fibers on top of them. Rectangle A: 19×15×2 mm. Rectangle B: 19×10×2 mm (length×width×height)

Table 3: Printing parameters of the HB- and PCL[1]-deposited fibers

	Pressure (MPa)	Speed (mm/min)	Voltage (kV)
Pneumatic-driven dispensing	0.060	5	-
MEW	0.120	15	-9.5

2.13 Statistics

The main available tests to perform a comparison of the mean values of different groups of data include the paired t-test, the independent t-test, the ANOVA-test, and the MANOVA-test. The paired t-test and the independent t-test are performed, while the mean values of only two groups of data are compared. The substantial difference among those tests is whether the comparing groups come from the same population (two outcome variables are examined) or not (same outcome variable is examined), respectively. The ANOVA-test and the MANOVA-test are used to compare the mean values of more than two groups of data. In the event the outcome variable is one, a ANOVA-test is optimal. Inversely, the MANOVA-test is suitable when at least two outcome variables are of interest.

In the study, all the results are expressed as mean value $\pm$ standard deviation. Moreover, the comparison among only two groups was performed based on a two-tailed (independent) t-test. The selection of a two-tailed t-test was made based on the assumption that the generated values follow normal distribution. Inversely, to identify differences between the means of multiple groups of interest, a one-way ANOVA post hoc Tukey test was executed. In all cases, the level of significance was set when $p < 0.05$. GraphPad Prism 8 software was utilized to perform the statistical analysis of the generated data.

Results

3.1 Assessment of the generated Python-code

The generated Python-code was able to replicate the morphology of the input .STL file. A qualitatively similarity exists between the actual .STL file and the respective graphs that were generated by the Python-code (Fig.21).

To validate the Python-code numerically, the minimum and maximum values of the coordinates prior and later of their manipulation by the Python-code were compared (Table 4). The values after the z-manipulation depicted the values while every z-coordinate lower than a constant equal to 0.5 was discarded. The selection of the particular constant helped to discard the coordinates that corresponded to the bottom closed surface of the .STL file. Subsequently, the MEW-printhead would not deposit material within the volume of the structure, leading to the crush of the nozzle. The extreme values while printing were different compared to those previously acquired. The main restriction was the efficiency of the refinement of the mesh, and secondly the deposition of fibers in a discrete fashion. For instance, the y_{max} value was different after thresholding the z-coordinates and while printing. This could be attributed to the insufficient refinement of the mesh since the difference between the y_{max} after the z-manipulation and that while printing was higher than the selected spacing of 0.2 mm. Inversely, the observed difference in x_{max} values was attributed to the selection of interfiber spacing.

Following, the percentage of achieved accuracy after each step of the Python-code was determined (Table 5). To estimate each type of accuracy (after the z-manipulation, while printing, the maximum due to the selected inter-fiber spacing, and the overall one), the formulae described in Equations 3, 4, 5, and 6 were used, respectively. In the case of the minimum values of coordinates, the maximum accuracy due to the selected spacing was not calculated since the MEW-printhead started depositing material at that point.

$$\text{Accuracy after z-manipulation } (\%) = \left(1 - \frac{\text{Real value} - \text{Value after z-manipulation}}{\text{Real value}}\right) * 100 \tag{3}$$

$$\text{Accuracy while printing } (\%) = \left(1 - \frac{\text{Value after z-manipulation} - \text{Value while printing}}{\text{Value after z manipulation}}\right) * 100 \tag{4}$$

$$\text{Maximum Accuracy due to the selected interfiber spacing } (\%) = \left(1 - \frac{\text{Spacing}}{\text{Value after z manipulation}}\right) * 100 \tag{5}$$

$$\text{Overall Accuracy } (\%) = \left(1 - \frac{\text{Real value} - \text{Value while printing}}{\text{Real value}}\right) * 100 \tag{6}$$

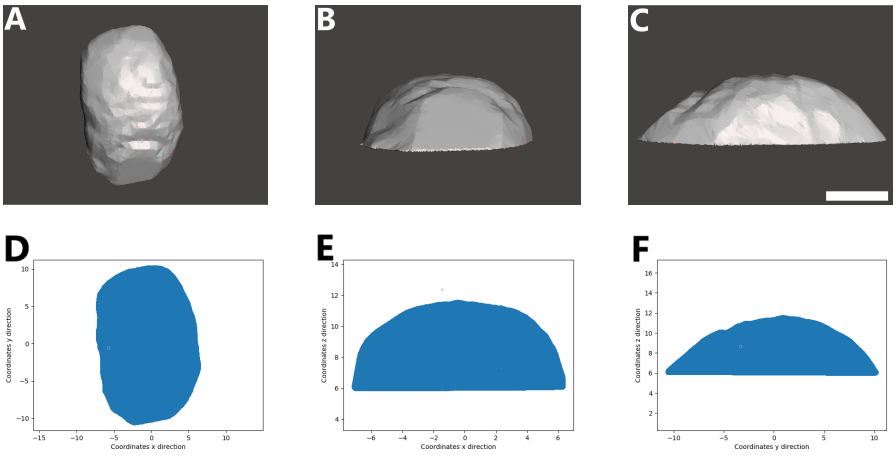


Fig. 21: Correspondence of the STL-file and the manipulated coordinates in the Python-code. A: Top view of human condyle (STL file), B: Back view of human condyle (STL file), C: Side view of human condyle (STL file), D: Top view of human condyle-Python-code, E: Back view of human condyle-Python-code, F: Side view of human condyle-Python-code. The scale-bar corresponds to 5 mm

Table 4: Numerical validation of Python-code

	Real values	Values after z-manipulation	Values while printing
y_{max}	10.201	9.917	9.665
y_{min}	-10.603	-10.254	-10.254
x_{max}	6.310	6.296	6.109
x_{min}	-7.112	-7.033	-7.033

The animation (Appendix 1.1, the animation is available only in a .PDF format, while in a hard copy-version a blank spot exists.) constitutes a recording of the movement of the MEW-printhead. Hypothetically, PCL[1]-fibers are deposited on top of the human condyle (Fig.21). A printing speed of 5 mm/min was selected.

Table 5: Percentage of accuracy of the generated G-code

	Accuracy after z-manipulation	Accuracy while printing ($\lesseqgtr$) Maximum accuracy	Overall accuracy
y_{max}	97.22%	97.46% $<$ 97.98%	94.75%
y_{min}	96.71%	100.00%	96.71%
x_{max}	99.79%	97.03% $>$ 96.82%	96.81%
x_{min}	98.89%	100.00%	98.89%

3.2 Fabrication of implants

The implants were successfully fabricated using both FDM and pneumatic-driven dispensing (Fig.22). The FDM-printing set-up resulted in implants characterized by an average fiber diameter ranging from 199 to 215 µm and pore size ranging from 582 to 606 µm (Table 6). The different printing set-ups of the pneumatic-driven dispensing also resulted in a narrow range of fiber diameter (from 285 to 314 µm) and pore size (from 404 to 444 µm), respectively.

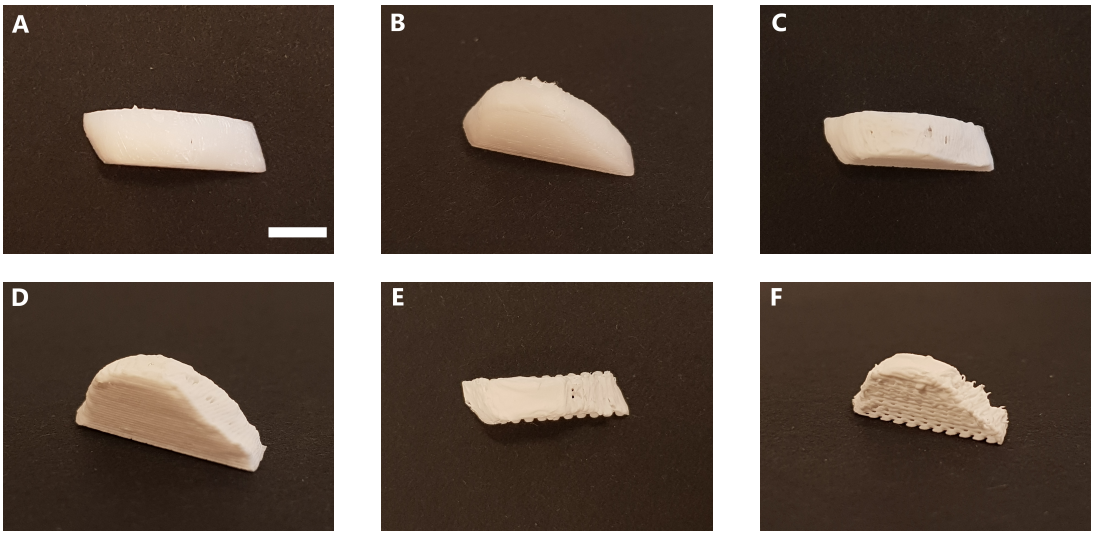


Fig. 22: The three different types of fabricated implants. A: Top view of implant III-(PCL[1]-shielded), B: Side view of implant III-(PCL[1]-shielded), C: Top view of implant III-(HB-shielded), D: Side view of implant III-(HB-shielded), E: Top view of implant III-(HB-porous), F: Side view of implant III-(HB-porous). The scale-bar corresponds to 5 mm

Table 6: Internal architecture of the fabricated implants

Implant Type	Average Fiber Diameter (μm)	Coefficient of Variation	Average Pore Size (μm)	Coefficient of Variation
PCL[1]-shielded	208±14	7%	593±25	4%
HB-shielded	297±12	4%	426±16	4%
HB-porous	301±8	2.7%	423±12	2.9%

The quite low ($< 10\%$) coefficients of variation indicate the consistency of the printing set-ups. To evaluate the accuracy of each method combined with the specific materials, measurements of the overall dimension fidelity of the implants were conducted. It was revealed that a high percentage of fidelity, ranging from 89.9±2.8% to 105.7±0.8%, was achieved (Fig. 23-E). Particularly, the PCL[1]-shielded implants presented a varying dimension fidelity from 95±5% to 105.7±0.8%. Also, the fidelity of HB-shielded implants ranged from 89.9±2.8% to 96.9±2.8%. The dimension fidelity of the HB-porous implants fluctuated from 93.0±2.2% to 100±9%.

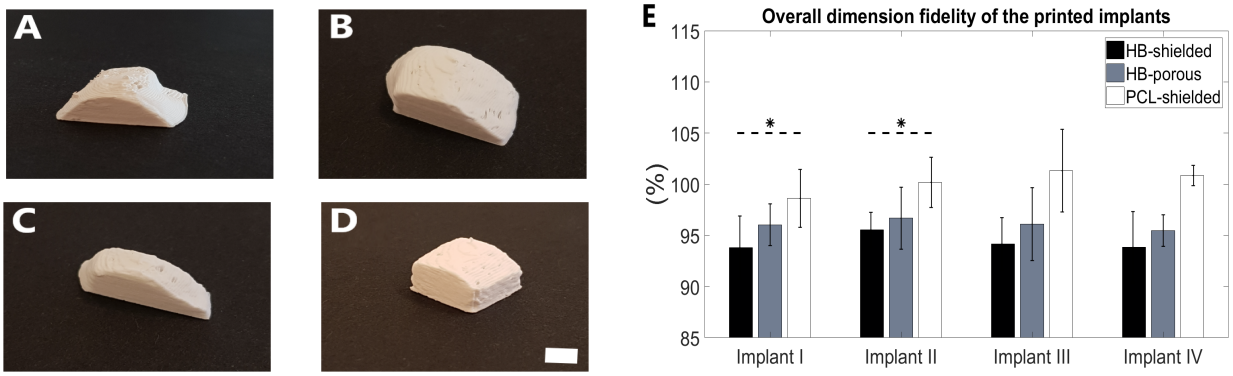


Fig. 23: A: Implant I (HB-shielded), B: Implant II (HB-shielded), C: Implant III (HB-shielded), D: Implant IV (HB-shielded), E: Comparing the percentage of fidelity in terms of size in the three dimensions of the fabricated implants. The scale-bar corresponds to 5 mm. $*$ indicates a significant difference, $p < 0.05$

3.3 Mechanical characterization of bulk materials

The apparent Young's modulus elasticity of PCL[1] and HB was measured under static compression (Fig.24). HB appears to endure high normal stresses without undergoing plastic deformation ($0.99 \pm 0.29 * 10^8$ Pa). The same applies for PCL[1] ($2.70 \pm 0.07 * 10^8$ Pa) (Fig.25). Yet, the CT-data revealed that the cast of HB was not completely filled (Appendix 1.2, the .mp4 file is available only in a .PDF format, while in a hard copy-version a blank spot exists). Therefore, the elastic Young's modulus of the bulk HB was underestimated. HB scaffolds presented a mostly uniform buckling effect while being loaded. Inversely, the PCL[1] one showed a characteristic sliding. To identify the correlation coefficient among the density of the bulk scaffolds and their Young's modulus elasticity (Fig.26), the first was considered as the independent variable while the second as the dependent. A correlation coefficient equal to $r_{PCL^1} = -0.00589$ and $r_{HB} = -0.0429$ was computed in the case of PCL[1] and HB, respectively.

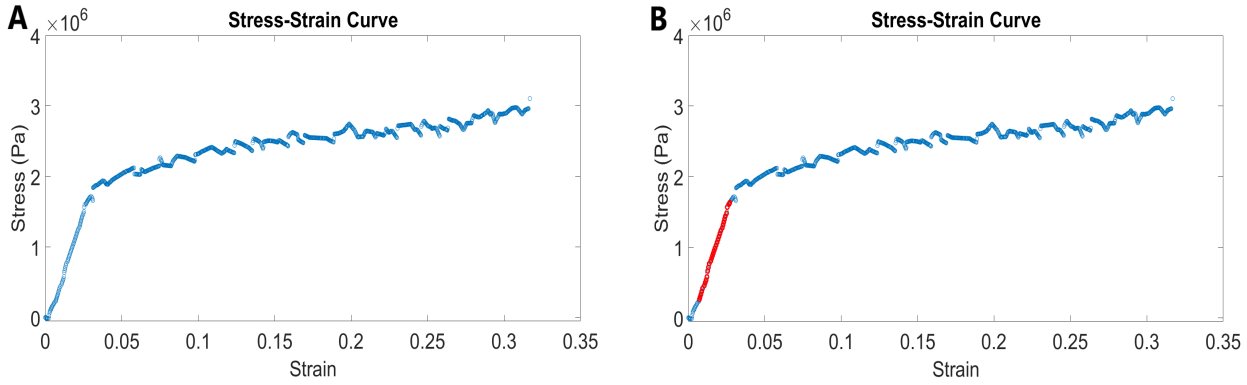


Fig. 24: A: The recorded force-displacement data were converted into stress-strain data, respectively. B: The Young's modulus elasticity was calculated based on the linear part of the slope of the stress-strain curve (red-marked data)

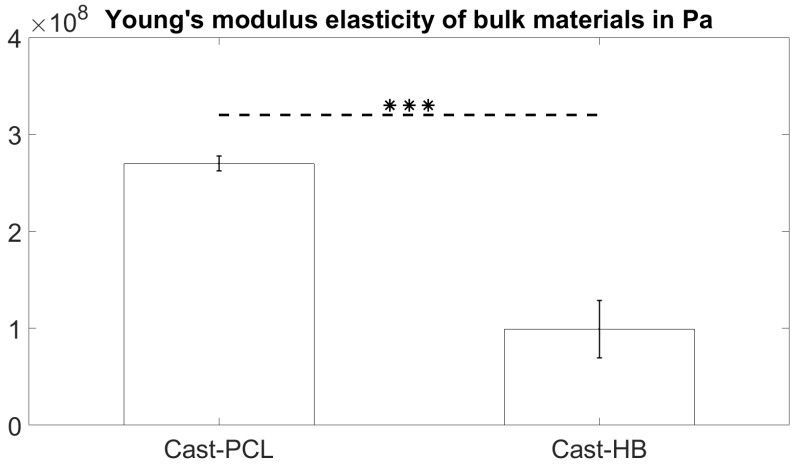


Fig. 25: Bulk properties of PCL[1] and HB materials. The compression elasticity of Young's modulus of the human trabecular bone, based on literature [75], is estimated to range from $1.41 * 10^9$ to $3.47 * 10^9$ Pa. $***$ indicates a significant difference, $p < 0.001$. No outliers were identified in the groups

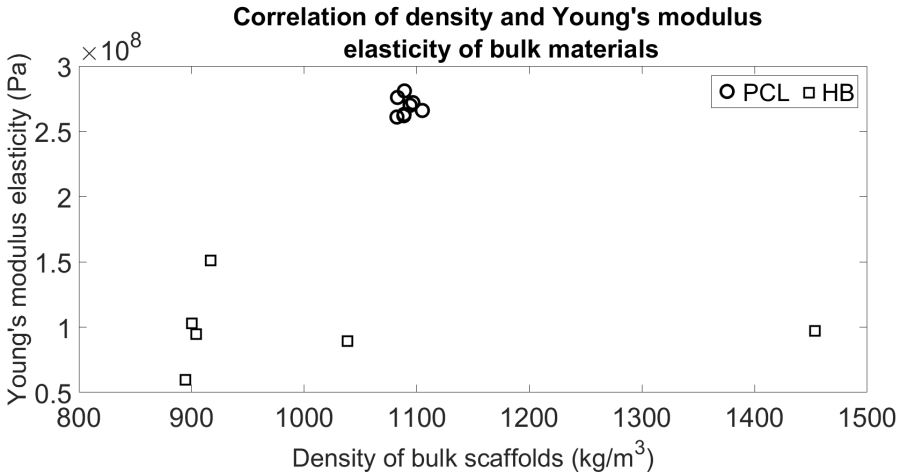


Fig. 26: The Young's modulus elasticity of the bulk scaffolds appears to scatter without a specific tendency relevant to their density

3.4 Mechanical characterization of HB-scaffolds

The different printing set-ups resulted in scaffolds characterized by an average diameter ranging from 260.8 to 331.4 µm. The average diameter was calculated to be 299±27 µm, resulting in a coefficient of variation of 9%. Respectively, the average pore size varied from 358.6 to 447.4 µm, resulting in an average pore size of 410±30 µm. The respective coefficient of variation was estimated to be 8%.

3.4.1 Role of design on scaffolds mechanical behavior The different types of scaffolds (Fig.27) were characterized mechanically under static uniaxial compression following the same protocol. In that way, the impact of each element (surrounding loop, and closed top layer) of the design on their mechanical behavior was examined. The biological requirements of the implant-design introduced those elements in the final design. Yet, they appear

not to affect the mechanical properties of the implants (Fig.28). Particularly, the “enclosed” scaffolds showed an Young’s modulus elasticity of $4.1 \pm 1.0 * 10^7$ Pa, the “encircled” $5.6 \pm 2.1 * 10^7$ Pa, and the “open” ones $2.9 \pm 1.3 * 10^7$ Pa. Significant difference was recorded between the “encircled”, and the “open” scaffolds.

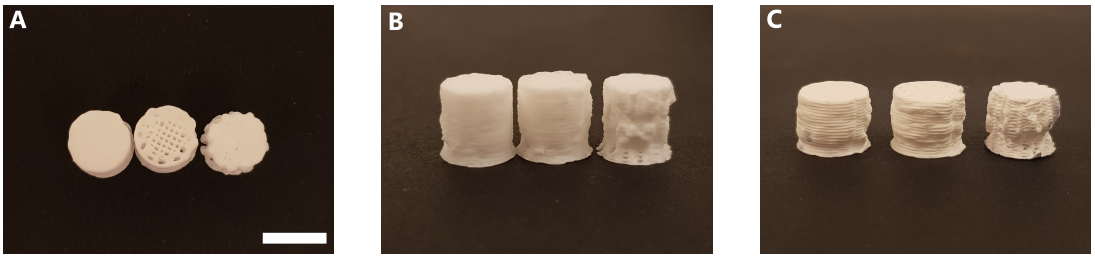


Fig. 27: Gross representation of the different fabricated designs (“enclosed”, “encircled”, “open” sides). A: Top view of undeformed HB-scaffolds. B: Side view of undeformed HB-scaffolds. C: Side view of deformed HB-scaffolds. The scale-bar corresponds to 8 mm

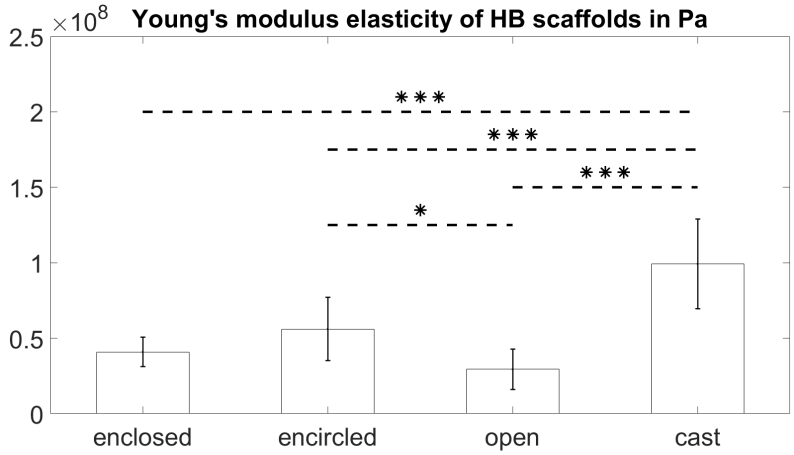


Fig. 28: Quantification of the Young’s modulus elasticity of HB-scaffolds designed following different patterns. $***$ indicates a significant difference, $p < 0.001$. $*$ indicates a significant difference, $p < 0.05$. No outliers were identified in the groups

3.4.2 Role of chondrogenic differentiation medium on scaffolds mechanical behavior Scaffolds that were cultured in chondrogenic differentiation medium for 28 days (“enclosed-28”) were compared with scaffolds that were not cultured (“enclosed”). After immersing the HB-scaffolds in chondrogenic differentiation medium and keeping them in culture conditions for 28 days (“enclosed-28” scaffolds), a comparable stiffness ($4.9 \pm 1.0 * 10^7$ Pa) to the non-cultured scaffolds ($4.1 \pm 1.0 * 10^7$ Pa) was reported (Fig.29). No significant difference was recorded between the two groups. The “enclosed-28” scaffolds were tested directly after their removal from the chondrogenic culture medium, while the “enclosed” scaffolds were completely dry. The absorbed medium in the “enclosed-28” scaffold was freely released during compressive loading, forming a droplet at the bottom compression plate (Appendix 1.3, the .mp4 file is available only in a .PDF format, while in a hard copy-version a blank spot exists).

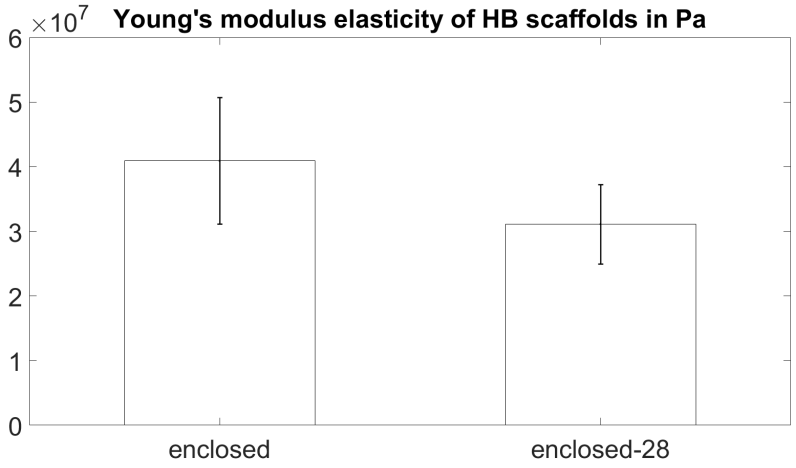


Fig. 29: The effect of pre-culture of the implant *in-vitro* in chondrogenic differentiation medium. No significant statistical difference was found among the examined groups. No outliers were identified in the groups

3.5 DLP *ex-vivo* model

The fabrication of the DLP-equivalent *ex-vivo* model was successfully accomplished. Both the intact femur, the tibia, the patella, and the defective femurs were fabricated.

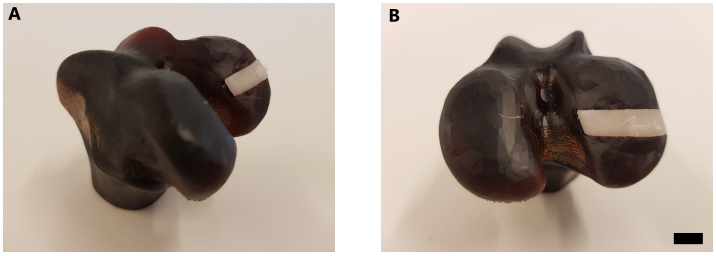


Fig. 30: The DLP equivalent of defect III and the corresponding PCL[1]-fabricated implant. A: Isometric view of defect III. B: Top view of defect III. The scale-bar corresponds to 5 mm

3.6 Deformation of implants in the DLP *ex-vivo* model

The majority of the load-deformation curves followed a particular pattern in the loading and the unloading phase (Fig.31). In the loading phase, the deformation increased along with the increased load with a rate that resulted in straight curves to the maximum load of 2000 N. Inversely, while unloading the recovering curve followed a different pattern. Initially the deformation decreased along with the decreased load with a rate of decline that did not result in a straight curve. Also, the unloading curve did not follow the exact same path. It returned close to the initial point following a path that, for the same load, a higher displacement was recorded. This resulted in the typical picture of an open hysteresis loop. The first circle of loading and unloading shows a slightly different pattern. This can be attributed to the fact that the measurements were performed while ensuring the correct positioning and attachment while testing. In that part there is no resistance of the implant. Thus, it constitutes a maligned period of testing.

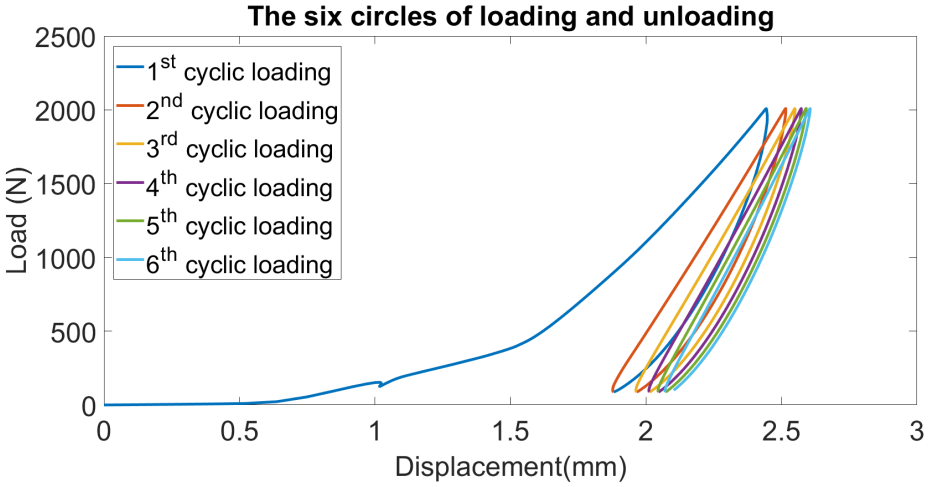


Fig. 31: Formation of the open hysteresis loop. The load-deformation curves of six circles of loading and unloading of the Implant I while being inserted in the DLP *ex-vivo* model. A 55° configuration was used

After completing the consecutive loading and unloading circles in the three different flexion angles, the process was performed again at the configuration of 55° of flexion. A drift of the hysteresis loops was noticed toward the smaller values of displacement (Fig.32). In the case of Fig.32, the average displacement at the maximum force was calculated to be 2.55 ± 0.06 mm, and 2.15 ± 0.05 mm in the first and the second repetition of the configuration of 55°, respectively. Taking also into consideration the fact that the unloading curve did not return to the initial point, it can be hypothesized that a permanent deformation or/and an accommodation of the implant inside of the DLP-model occurred.

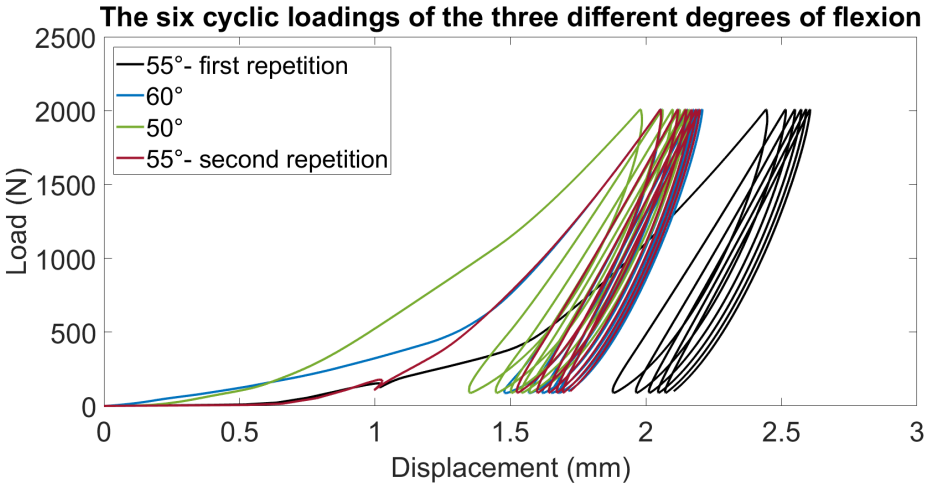


Fig. 32: The fabricated implants present a degree of plasticity. The figure shows the load-deformation curves of six circles of loading and unloading of the Implant I while being inserted in the DLP *ex-vivo* model. All the configurations of flexion are presented. The second repetition at the configuration of 55° of flexion demonstrates constantly smaller values of deformation

The average displacement at the maximum force in the case that the implants were placed at the defective femur was calculated (Table 7). The presented values were calculated based on the last repetition of each configuration. Particularly, Implant I presented an average displacement of 2.07 ± 0.07 mm, Implant II 1.46 ± 0.13 mm, Implant

III 1.05 ± 0.04 mm, and Implant IV 1.29 ± 0.15 mm at the configuration of 50°. A similar trend was recorded in the 55° configuration. Implant I showed an average displacement of 2.16 ± 0.05 mm, Implant II 1.73 ± 0.11 mm, Implant III 1.027 ± 0.024 mm, and Implant IV 1.32 ± 0.9 mm. Moreover, the average displacement was recorded to be 2.16 ± 0.05 mm in Implant I, 1.54 ± 0.09 mm in Implant II, 1.01 ± 0.06 mm in Implant III, and 1.32 ± 0.17 mm in Implant IV at the configuration of 60°. The low coefficients of variation indicate the consistency of the testing process.

Table 7: Average displacement(mm) at the maximum force for the defective femur to the tibia configuration, with the implant placement

Degrees of flexion (°)	Implant I	Coefficient of Variation	Implant III	Coefficient of Variation
50	2.07 ±0.07	3%	1.05±0.04	4%
55	2.16± 0.05	2%	1.027±0.024	2%
60	2.16±0.05	2%	1.01±0.06	6%
Degrees of flexion (°)	Implant II	Coefficient of Variation	Implant IV	Coefficient of Variation
50	1.46±0.13	9%	1.29 ± 0.15	12%
55	1.73±0.11	7%	1.32±0.09	7%
60	1.54 ±0.09	6%	1.32±0.17	13%

Concerning the observed hysteresis loops, the area enclosed by the loop indicates the dissipated energy (U_d) in the particular cyclic loading (Fig.33). While, the elastic energy (U_e) is illustrated by the area under the recovery curve (black-shaded area). The summation of the two types of energy corresponds to the total energy (U). To calculate the dissipated and the elastic energy, the trapezoidal rule was applied. Since the fabricated implants have different dimensions, the parameters of study were selected to be the energy ratios U_d/U and U_e/U. In that way, both the dissipated and the elastic energy were normalized by the dimensions of the implants (Table 8).

The normalized elastic energy stored in Implant III was significantly greater (Fig.34), and, inversely, the normalized dissipated energy was significantly smaller than Implant I (Fig.35) at all the configurations of flexion. Particularly, the normalized elastic energy of Implant I versus Implant III was calculated to be 0.68±0.04 versus 0.772±0.028, 0.71±0.03 versus 0.783±0.021, 0.70±0.03 versus 0.781±0.021, in the configuration of 50, 55, and 60° of flexion, respectively.

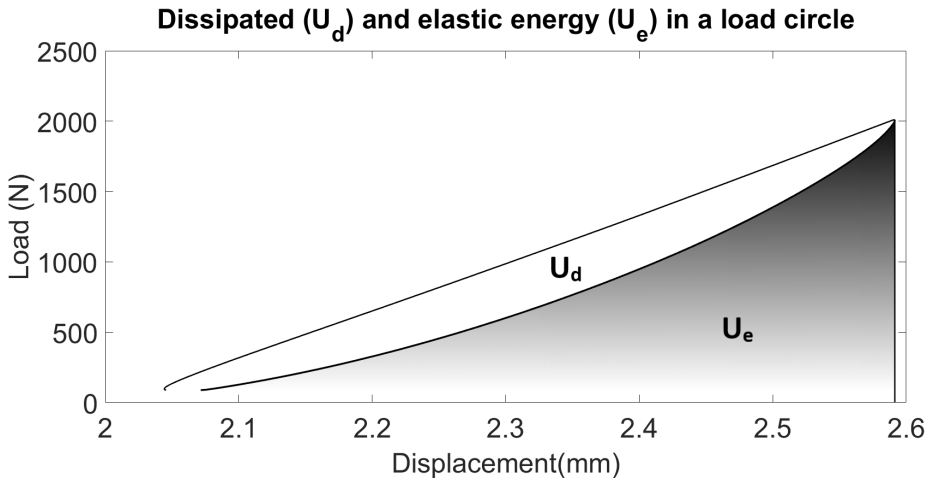


Fig. 33: Elastic (U_e), and dissipated energy (U_d) in a load cycle

There was no significant difference systematically between Implant I and Implant II. Particularly, the normalized elastic energy of Implant I versus Implant II was calculated to be 0.68±0.04 versus 0.73±0.04, 0.71±0.03 versus 0.74±0.03, 0.70±0.03 versus 0.74±0.04, in the configuration of 50, 55, and 60° of flexion, respectively. The normalized elastic energy derived from Implant II, and Implant IV were not statistically different. The calculated values of Implant II versus Implant IV were 0.73±0.04 versus 0.75±0.03, 0.74±0.03 versus 0.754±0.026, 0.74±0.04 versus 0.759±0.029 in the configuration of 50, 55, and 60° of flexion, respectively.

Table 8: Energy ratios. The average total energy (U), the average ratios of the elastic energy (U_e), and the dissipated energy (U_d) per loading/unloading circle. The outliers were removed to calculate the average values

Type of Implant	Degrees of flexion (°)	U (N mm)	Coefficient of Variation	U_e/U	Coefficient of Variation	U_d/U	Coefficient of Variation
Implant I	50	680±60	9%	0.68±0.04	6%	0.32±0.04	12%
	55	580±30	6%	0.71±0.03	5%	0.29±0.03	12%
	60	600±40	7%	0.70±0.03	5%	0.30±0.03	11%
Implant II	50	520±40	8%	0.73±0.04	5%	0.27±0.04	13%
	55	480±40	8%	0.74±0.03	4%	0.26±0.03	13%
	60	490±70	13%	0.74±0.04	5%	0.26±0.04	15%
Implant III	50	446±28	6%	0.772±0.028	4%	0.228±0.028	12%
	55	401±19	5%	0.783±0.021	3%	0.217±0.021	10%
	60	411±16	4%	0.781±0.021	3%	0.219±0.021	10%
Implant IV	50	414 ±28	7%	0.75±0.03	4%	0.25±0.03	12%
	55	460±80	17%	0.754±0.026	3%	0.246±0.026	10%
	60	410±23	6%	0.759±0.029	4%	0.241±0.029	12%

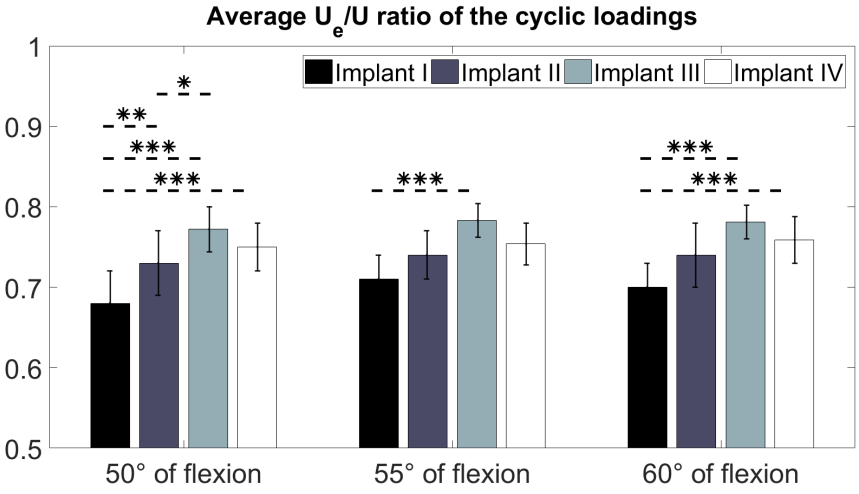


Fig. 34: The average normalized elastic energy of the different implants in the three degrees of flexion. $***$ indicates a significant difference, $p < 0.001$. $**$ indicates a significant difference, $p < 0.01$. $*$ indicates a significant difference, $p < 0.05$

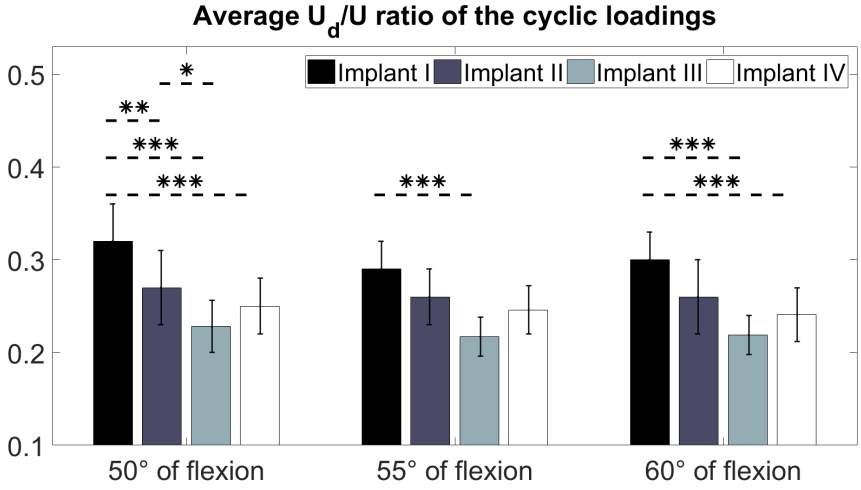


Fig. 35: The average normalized dissipated energy of the different implants in the three degrees of flexion. $***$ indicates a significant difference, $p < 0.001$. $**$ indicates a significant difference, $p < 0.01$. $*$ indicates a significant difference, $p < 0.05$

To calculate the average contact stress in each case, the contact area was estimated in each configuration (Fig.36). Particularly, the contact area was measured to be 175 mm^2, 100 mm^2, 20 mm^2 in the 50, 55, and 60° of flexion, respectively. Following this, the contact stresses at the maximum force were calculated (Fig.37). A statistically significant difference was demonstrated in each implant among the three different degrees of flexion. Yet, no significant difference was observed among the contact stresses of the different implants in the same configuration. Particularly, Implant I showed average contact stress of 11479300±2400, 20088000±6000, 100437000±20000 Pa in the configuration of 50, 55, and 60° of flexion, respectively. In the case of Implant II the average contact stress was calculated to be 11479200±1800, 20089000±6000, 100438000±22000 Pa in the configuration of 50, 55, and 60° of flexion, respectively. Regarding Implant III, at 50° of flexion the contact stress was estimated to be 11482400±2000, at 55° 20091000±3000, and at 60° 100451000±19000 Pa. Implant IV showed average contact stress of 11477900±2400, 20088000±4000, 100437000±22000 Pa in the configuration of 50, 55, and 60° of flexion, respectively.

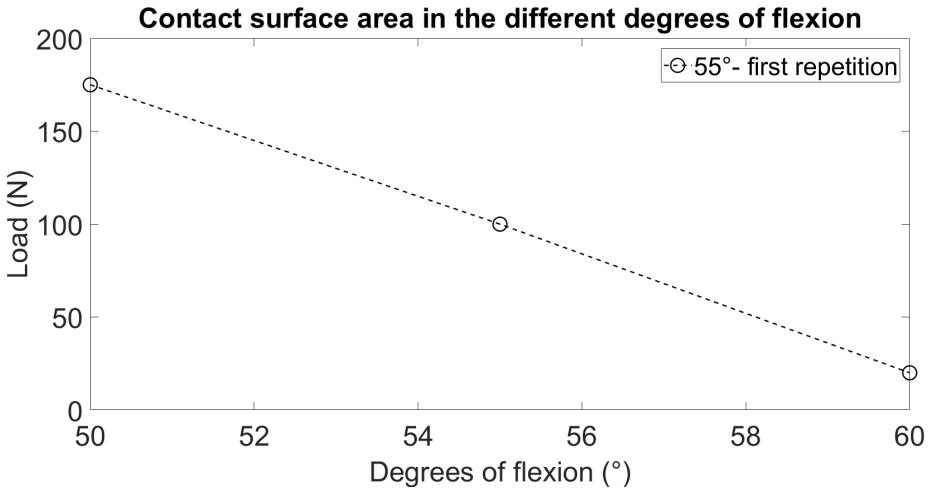


Fig. 36: The contact area decreases as the degree of flexion increases

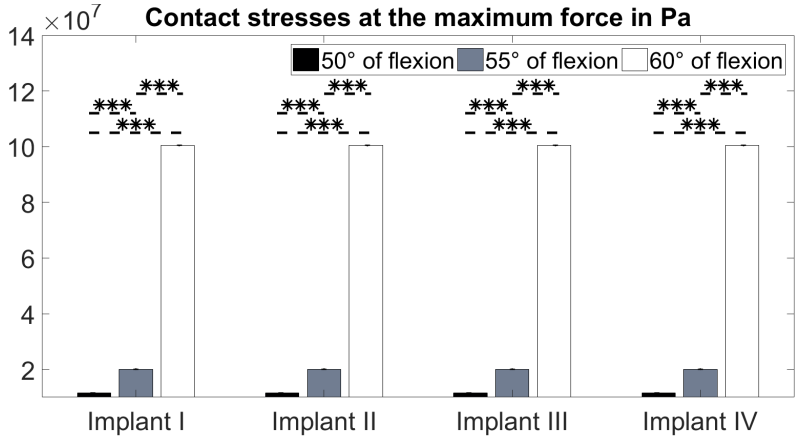


Fig. 37: The contact stress at the maximum force. There was not identified a statistically significant difference among the different implants in the same degrees of flexion. Statistical difference was identified among the different degrees of flexion of the same implant. $***$ indicates a significant difference, $p < 0.001$

Finally, the height-deformation of the tested implants was measured. The values of deformation were recorded as following: 0.75±0.07mm, 0.63±0.25mm, 0.4±0.14mm, and 0.2±0.17mm in Implant I, Implant II, Implant III, and Implant IV, respectively.

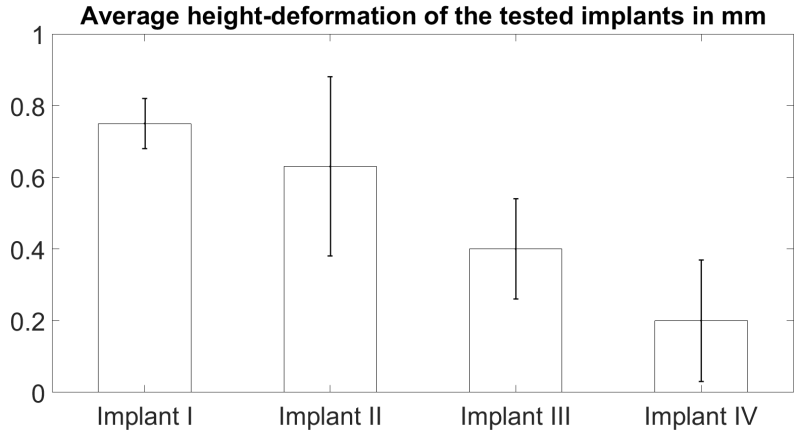


Fig. 38: The average height-deformation of the tested implants. No outliers were identified in the groups. No significant statistical difference was found in the examined groups

3.7 Microscopical characteristics of fused fibers

Fusion and microscopical characteristics of the deposited HB- and PCL[1]-fibers using pneumatic-driven dispensing and FDM, respectively, were characterized by SEM analysis (Fig.39) In all the cases, each layer was fused with the previously deposited layer. Moreover, the $Mg_3(PO_4)_2$ nano-particles were obvious both in the top and the side view of the HB-deposited fibers, resulting in textured HB-deposited fibers, compared to the PCL[1]-deposited fibers that were much more smoother.

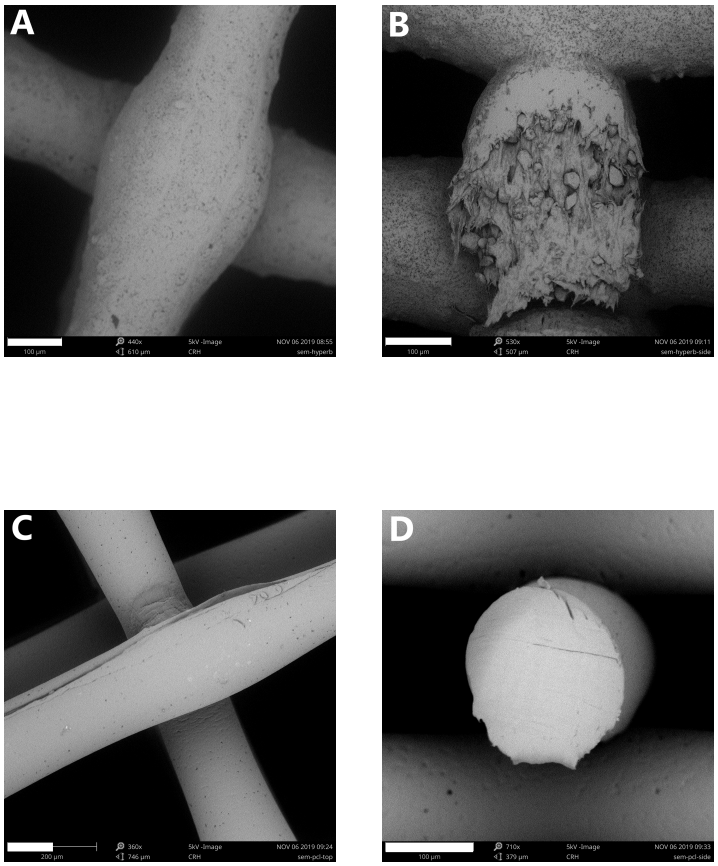


Fig. 39: Microscopical characteristics of the deposited fibers within two different types of samples. (A): Top view of the HB-deposited fibers via pneumatic-driven dispensing, (B): Side view of the HB-deposited fibers via pneumatic-driven dispensing, (C): Top view of the PCL[1]-deposited fibers via FDM, (D): Side view of the PCL[1]-deposited fibers via FDM. The scale-bars correspond to 100 µm. The applied voltage was set at 5 kV

One of the ways to fabricate a cartilaginous compartment is to generate reinforced hydrogels using a thermosensitive polymer, as PCL[1]. Therefore, the attachment and the fusion of HB (oseous compartment) and PCL[1] (cartilaginous compartment) were examined by SEM (Fig.40). Pneumatic-driven dispensing, and MEW were used to deposit the respective materials. Three different time points of elapsed printing time of MEW-PCL[1] fibers were evaluated: the starting time-point (t=0 sec), the finishing time-point (t=t_1=25 sec) of the Rectangle B (Fig.20), and the finishing time point (t=t_2=45 sec) of the Rectangle A (Fig.20). It is evident that there was an organized deposition of the PCL[1]-fibers on top of the HB compartment. A non-homogeneously porous structure was revealed by SEM. This is accurate both in the starting and the finishing time-points, at t=0 and t=t_2 (Fig.39-A, B), respectively. The designed deposition of the PCL[1]-fibers should have resulted in a homogeneous box-architecture. The inter-fiber spacing was set at 400 μm. However, due to the inconsistencies of deposition of the HB, the inter-fiber spacing was measured to be 310±70 μm, and 310±60 μm in the starting and the finishing time-points, at t=0 and t=t_2 (Fig.39-A, B), respectively. Moreover, due to these inconsistencies, sites of attached and sagging fibers can be observed (white arrows in Fig.39-B). ImageJ was used to quantify the inter-fiber spacing, and the total thickness of the PCL[1]-mesh.

Since the intersections of the MEW-mesh are responsible for taking up the majority of the stresses in a reinforced hydrogel [76], they were examined closely. As can be seen, the deposition is accurate to a good extent also in the intersections. There is no apparent tension on the MEW-fibers. Ten layers of MEW-fibers were printed, resulting in a height of approximately 30-50 µm. The particular height seems to be insufficient to create difference of height in the cross-sections (Fig.39-C, D).

Regardless of the elapsed printing time, there are sites of attachment between the HB-deposited surface and the first layer of deposited PCL[1]-fibers (Fig.39-C, E, F). Thus, a bonding between the osseous and the partially cartilaginous compartment was achieved.

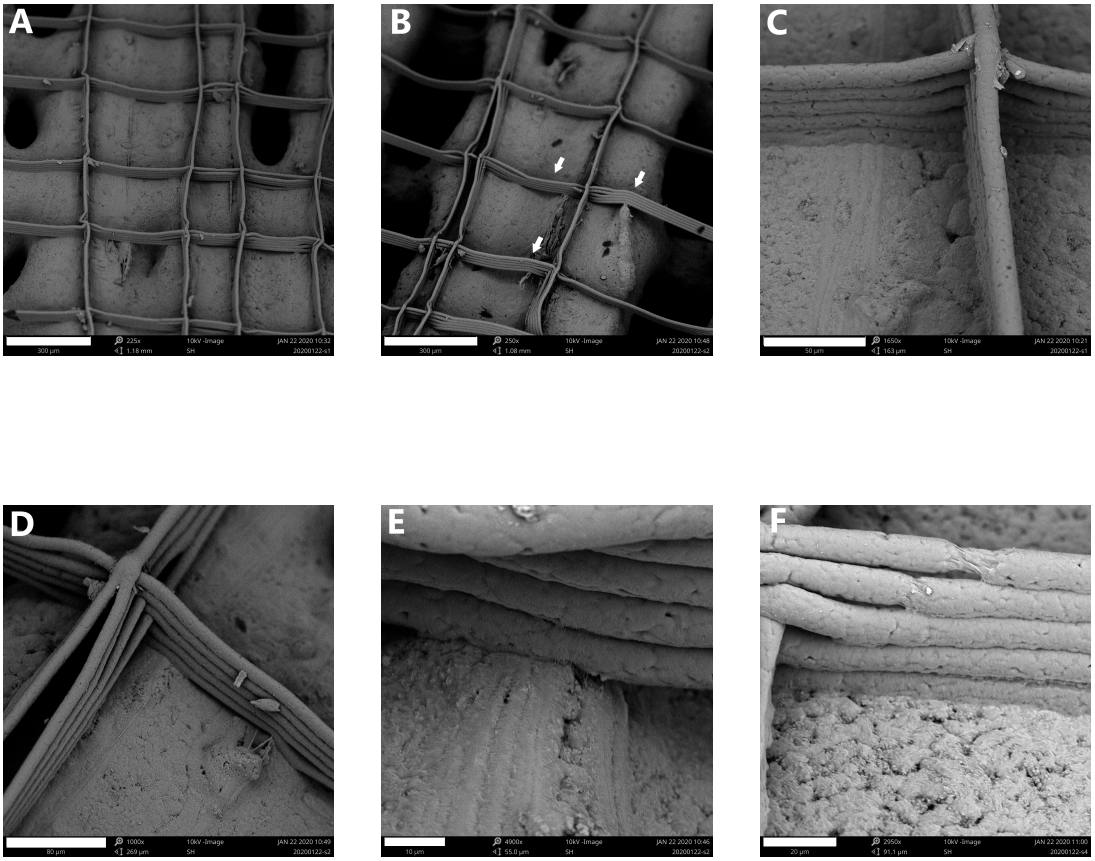


Fig. 40: Microscopical characteristics of the PCL[1] deposited fibers (MEW) on top of a HB-surface (pneumatic-driven dispensing). A: Angled view (45°) of PCL[1]-deposited fibers at t=0. The scale-bar corresponds to 300 µm, B: Angled view (45°) of PCL[1]-deposited fibers at t=t_2. The scale-bar corresponds to 300 µm, C: Angled view (45°) of PCL[1]-deposited fibers at t=0. The scale-bar corresponds to 50 µm, D: Angled view (45°) of PCL[1]-deposited fibers at t=t_2. The scale-bar corresponds to 80 µm, E: Angled view (45°) of PCL[1]-deposited fibers at t=t_2. The scale-bar corresponds to 10 µm, F: Angled view (45°) of PCL[1]-deposited fibers at t=t_1. The scale-bar corresponds to 20 µm, The applied voltage was set at 10 kV

Comparing the morphology of the PCL[1] fibers via FDM (Fig.39-C) and MEW (Fig.40-F), a non-similar texture is observed. Notably, the MEW-PCL[1] fibers appear more textured compared to the FDM-PCL[1] ones. In both techniques, the material was heated to ensure a proper viscosity. However, the driving force in MEW constitutes a tensile force, while a compressive force takes place in FDM. Therefore, the FDM-deposited fibers are more smooth and dense compared to the MEW-deposited ones.

Discussion

The convergence of MEW, and extrusion-based techniques has already been reported [42]. Yet, to the best of my knowledge, there are no previously published studies introducing the ability to deposit MEW-fibers of material on top of any non-smooth and concave surface. The accuracy of the movement of the print-head was higher than 94.75% in all the directions of movement. However, the accuracy was found to be dependent on the selected inter-fiber spacing and the efficiency of the refinement of the corresponding .STL file.

The implants were successfully fabricated using both of the available techniques. Although no significant differences were found systematically, pneumatic-driven dispensing (HB) seems to result in smaller implant size as compared to the programmed size, whereas FDM (PCL^1) seems to lead to slightly over-sized implants, respectively. It is to be noted that these discrepancies are not only technique-dependent. The used material (HB and PCL^1 respectively), and the way of fusion/solidification of the subsequent layers is also important. Therefore, these results cannot be considered to evaluate the dimension fidelity of the techniques in a comparable way, although they constitute valuable data for future optimization. Interestingly, the dimensions of the HB-porous implants were comparable to those of the HB-shielded. One would expect the first ones to be significantly smaller, based on the scaling process by 97% that was followed to design them.

Commonly in literature the HB is referred as the combination of PCL^1 and HA^2. In our case-study, HA^2 was replaced by $Mg_3(PO_4)_2$. As has been discussed in the introductory chapter, the growth factors used in bone regeneration are characterized as non-cost-efficient since the relevant clinical results are dubious. Advances in the material-science field have been reported. The inclusion of magnesium in growth factor-free inks for bone regeneration could be prosperous. Magnesium (Mg) constitutes a bioinorganic that has been proven to be substantial in bone development. Compared to other biodegradable metals such as iron (Fe) and zinc (Zn), Mg seems to be more suitable. The daily intake of Mg is quite higher (about 50 times) than that of Fe and Zn. Also, it has been reported that a higher intake of Zn could be life-threatening. Hence, the human organism has a greater extent of resilience to Mg [46]. Additionally, the release of ions could play a critical role to the adjustment of the pH toward neutral values. It has been shown that micro-particles of degraded magnesium lead to the formation of magnesium hydroxide, which constitutes a main component of antacids in already approved and available medicines. Hence, it can neutralize or increase the pH, while the polymer degradation creates an acidic environment. Particularly, magnesium in a watery environment (H_20) follows the chemical reaction:

$$Mg + H_20 \rightarrow Mg(OH)_2 + H_2,$$

leading to an increase of the pH (alkaline environment). Hence, an antibacterial and osteogenic differentiation-friendly environment is created. Both the products of the chemical reaction can be processed by the human body. Particularly, magnesium hydroxide ($Mg(OH)_2$) can be processed and removed via urine, while hydrogen gas (H_2) can be removed by the lungs [46].

HB, as a composite of PCL^1 and magnesium phosphate ($Mg_3(PO_4)_2$) should demonstrate superior stiffness compared to PCL^1. Yet in the particular case-study, it shows inferior stiffness. This observation constitutes an indication that the voids that were generated during the casting significantly affected the measured stiffness. Despite the dominant ceramic component of the HB-ink, it presented an elastic area of deformation. It has been reported that, on average, the osteochondral interface in adults is approximately three mm. Particularly, articular cartilage compromises the main body (90%), while calcified cartilage and subchondral bone covers the rest equally [16]. Therefore, the subchondral bone has a height of about 0.15 mm. Hence the created defects in the epiphysis of the femur in the current work consisted of the subchondral bone and the trabecular bone at a percentage of 2.5% and 97.5%, respectively. In the epiphysis, the cortical bone is constrained into a thin layer [16]; therefore, the assumption that 97.5% of the defect consisted of trabecular bone can be justified. Hence, the results of the mechanical characterization in the study were compared to the stiffness of the trabecular bone reported in the literature. The implants should show adequate mechanical properties as they are implanted till the remodeling process of the tissue is completed. The results indicated that the bulk compressive stiffness of HB was quite lower than that of trabecular bone. Moreover, in a clinical application, the specification of each patient should be taken into account. For instance, the age, the sex, the weight, and clinical-history of each patient are parameters that

affect the remodeling process [46]. The data of the density and the Young's modulus elasticity of the bulk materials presented a greater scattering in the case of HB than PCL[1]. However, in both cases it appears that there is no strong correlation between the Young's modulus elasticity and the calculated density.

Additionally, the "enclosed", the "encircled", and the "open" scaffolds all presented similar Young's modulus elasticity. As expected, the cast-scaffolds showed significantly higher compressive stiffness than any other scaffold type. Following, the effect of *in-vitro* conditions was examined. It was not possible to quantify any significant difference. However, the "enclosed-28" were tested in wet conditions, while the "enclosed" ones were dry. The specific choice was made to emulate the following protocol regarding the implantation of implants in an *in-vivo* study. One could argue that the calculated stiffness of the "enclosed-28" scaffolds was overestimated because of the liquid phase. To elaborate, the fluid pressure acts actually as a fluid load support, uptaking most of the pressure. This resulted in removing liquid from the sample. A tissue equivalent that this phenomenon occurs is the articular cartilage. However, this discrepancy would be of high significance in the case that the compression test was held in a confined environment, as in the case of articular cartilage.

The results derived from the *ex-vivo* testing system demonstrated a permanent deformation of the PCL[1]-fabricated implants. In the particular case-study, the impact of the width and the confinement of the implants was investigated. Comparing the energy ratios of U_e/U, and U_d/U, it was demonstrated that there is no systematic significant difference between Implant II and Implant III. Whereas, there was a statistically significant difference between Implant I and Implant III in all the degrees of flexion. These data indicate that the width of Implant II might constitute the critical size regarding the joint congruity. The same indices could be used to examine the effect of the confinement of the implant from the surrounding material. The results of Implant II and Implant IV did not present significant statistical difference. However, the total deformation in height of the implants after the completion of the cyclic loadings was comparable. Thus, the main reason that resulted in significantly different energy ratios seems to be the accommodation of the implants in the joint. Ideally, there should not be any motion between the implant and the defective femur. Yet, there was not any means of fixation of the implants.

Also, the SEM analysis of the different samples indicated that the micro-architecture of each fiber is not dependent solely on the used biomaterial. Furthermore, the printing technique contributes to the final texture. Structural continuity at the interface of an osseous- and a cartilaginous-compartment was achieved between the HB surface and the PCL[1] layer. It constituted an effort to fabricate a single but non-homogeneous scaffold. Hence, no sutures were applied. The continuity was achieved through the fusion of the two materials. The already deposited MEW-fibers were firmly stuck and became one part with the underlying HB surface. To decrease the sagging of the deposited fibers, one solution could be the increase of the attachment surface area. Practically, to increase the diameter of the deposited fibers. By increasing the melting temperature, the viscosity of PCL[1] is decreased. Hence, PCL[1] shows a decreased resistance to be extruded as well. Maintaining the other parameters the same, a larger amount of mass is deposited, resulting in fibers with larger diameter [33]. Also, to decrease the sagging effect, especially close to the intersection points, an increase of the collector speed could be beneficial. As the speed increases toward the critical translation speed (CTS), the point of deposition matches the position of the spinneret. Hence, a decreased jet lag is observed [33]. Also, a smaller inter-fiber spacing could lead to fewer sagged fibers since it would provide the fibers being deposited with more attachment sites to the already deposited fibers.

Future Suggestions

Based on the challenges and the findings of the current study, a few more aspects can be examined in the future. Starting from convergence of MEW and extrusion-based techniques, the Python-code should be adapted in a way to be able to create a mat of crossed fibers. As has been shown in the case of MEW-reinforced hydrogels, designing the superficial zone of articular cartilage as a mat of crossed fibers (0-45-90-135° lay-down pattern), and the middle and deep zone as a uniform box architecture (0-90° lay-down pattern) is beneficial. Superior achieved peak modulus has been recorded [76]. In the particular study, a top-down printing method was followed to achieve the fabrication of the construct in one print and, more importantly, to ensure that the two micro-architectures were sufficiently fused. In the case of osteochondral implants, this approach is not practical. Hence, a gradient from larger inter-fiber spacing to smaller one in the superficial zone could ensure the attachment of the layers being printed to the previously deposited ones.

Moreover, regarding the fabrication of the implants, the protocol of the synthesis of the HB ink should be optimized. Stirring by hand results in viscosity inconsistencies of the ink, which can affect the fiber diameter and the pore size of each batch of material. To overcome this, an automated process should be followed (e.g., use of rolling plate or sonication under a chemical hood). An encountered difficulty through the project was the fabrication of shielded implants at the sides of the knee joint space and, at the same time, porous at the interface with the native bone. To overcome this, the available software should be developed from the respective company considering the needs of design in biofabrication.

Regarding the mechanical characterization of HB under compression, a dynamic loading condition could also be examined instead of a static approach. In daily-life activities (e.g., jumping) dynamic loading conditions are demonstrated. A disadvantage of the HB formulation is the high content of ceramic which might result in propagation of potential micro-fractures. Moreover, the static compression tests have shown the impact of the implant design on the Young's modulus elasticity. The tested scaffolds were composed of one closed top layer. However, in patient-specific implants, the number of the closed top layers will be dependent on the exact geometry of the implant. A prospective study could indicate the number of the closed top layers, which can result in a statistically significant difference in the stiffness of the implants. Particularly, the optimal index of the study could be the ratio of the height of the closed top layers to the height of the whole scaffold. Moreover, the chondrogenic differentiation medium in the pre-culture period seems not to affect the stiffness of the HB-scaffolds. A period of 28 days constitutes the key pre-culture period prior to the *in-vivo* implantation of a cartilaginous implant. Also, cells need to be included in the cartilaginous compartment of an osteochondral implant. In the pre-culture period, ions from the HB scaffolds are released in the chondrogenic differentiation medium. Therefore, a cell study should be considered. The aim would be to investigate how the cell proliferation, and differentiation toward the chondrogenic lineage can be affected from the concentrations of released ions.

The results regarding the joint congruity of the study are dependent on the material of the DLP *ex-vivo* model. Hence, using the same protocol to test the same gross geometries in the same native ovine stifle could enable the comparison of the two *ex-vivo* systems. The executed analysis generated results in discrete angles of part of the range of the stifle joint flexion. Therefore, another possibility would be to perform a similar analysis with continuous angles raging from the stand phase to the full flexion. However, in this case, both the gait pattern and the joint differences should be meticulously taken into consideration. Similarities have been recorded in the gait pattern. Both the human and the ovine joint flex, extend, and flex and extend while they are loaded, prior to toe-off and while being in the swing phase, respectively. Yet, the range of flexion in each model is significantly different [69].

Additionally, gross-geometries of the osseous implant that diminish the amount of the removed healthy tissue should be examined. In that case, a finite element model (FE) validated by the acquired experimental data could be useful. Reliable predictions of how different gross sizes and geometries, and different internal architectures of the implants, can affect the knee joint integrity could be acquired. Particularly, the distribution of the stresses on the surface of the implant and the resulting deformation could be assessed. In that way, the need of laboratory facilities and experimental data could be decreased slightly. However, the cases of high interest of the *in-silico* model should be experimentally examined.

Finally, the fusion of PCL^1 (MEW) on top of a flat surface of HB (pneumatic-driven dispensing) was examined. Further to the visual attachment of the osseous (HB) and cartilaginous (PCL^1) compartment, the interfacial

adhesion strength of the two surfaces could be quantified. That actually suggests performing a shear test. However, to apply a purely shear load, a custom-designed clamp should be fabricated. Additionally, the height of the HB-rectangles could be increased to 6 mm to imitate the height of the fabricated implants. In that case, the possible electrical isolation could also be investigated. Also, taking advantage of the generated Python-code, the fusion of PCL[1] (MEW) on top of a concave and non-smooth surface of HB (pneumatic-driven dispensing) could be evaluated.

Conclusions

The research aims of the current work were the following: (1) converge MEW and extrusion-based techniques; (2) introduce biologically and mechanically functional large osteochondral implants; (3) determine the stiffness of osseous implants in respect to the proposed design and the *in-vitro* pre-culture conditions; (4) evaluate the correlation between the size and confinement of osseous implants to their mechanical stability; (5) assess the extent of fusion of the compartments of a single but heterogeneous osteochondral implant.

Generating the Python-code, the convergence of MEW and extrusion-based techniques was successfully achieved. Yet, the efficiency of the code is strongly dependent on the level of mesh refinement of the used .STL file. Moreover, the implants were successfully printed using two different design approaches. It was shown that the stiffness of each implant was not strongly related to the following design approach. Particularly, the fabricated periphery loop and the closed top layer did not have any significant impact on the stiffness under compression. Moreover, the *in-vitro* pre-culture period did not decrease the stiffness of the implants. However, the Young's modulus elasticity of bulk HB appears to be lower than that of native trabecular bone. Following, the integrity of the knee joint was demonstrated to be slightly affected by the width of the implants. The confinement of the implant by the surrounding material had no effect. In terms of the size of the created defect, the results indicate that the width of 10 mm seems to be critical. Regarding the fusion of HB and PCL[1], this resulted in non-homogeneous porous structures on top of the HB surface. Moreover, the fusion at the interface was demonstrated to be related to the material inconsistencies of the HB-surface. No solid conclusion can be derived regarding the extent of fusion and the elapsed printing time.

Acknowledgments

The author acknowledges Mylène de Ruijter and Mohammad Mirzaali Mazandarani. Their expertise in osteochondral biofabrication and biomechanics was valuable to revise the content of the report. The contribution of Miguel Castilho was crucial to coordinate the experimental sections, both in The Netherlands and Australia. In addition, the help of Roderick Verberne was valuable. Moreover, I would like to mention additional help from Quentin Clément Peiffer, Paweena Diloksumpan, Mauricio Cruz Saldivar, Nasim Golafshan, and Paulina Nuñez Bernal.

Conflict of Interest

No commercial or financial affiliation/alliance was involved in the current study that could presume conflict of interest.

References

[1] Mouser V H M, A Abbadessa, R Levato, W E Hennink, T Vermonden, D Gawlitta, and J Malda. n.d. "Development of a Thermosensitive HAMA- Containing Bio-Ink for the Fabrication of Composite Cartilage Repair Constructs Development of a Thermosensitive HAMA-Containing Bio-Ink for the Fabrication of Composite Cartilage Repair Constructs." IOP Publishing.

[2] World Health Oragnization, Chronic diseases and health promotion `https://www.who.int/chp/topics/rheumatic/en/`

[3] Bichara David A, Hatice Bodugoz-sentruk, Doris Ling, and Erik Malchau. 2014. "Osteochondral Defect Repair Using a Polyvinyl Alcohol-Polyacrylic Acid (PVA-PAAc) Hydrogel." https://doi.org/10.1088/1748-6041/9/4/045012.

[4] Kingdom, United. 2010. "Stem Cells and Cartilage Development : Complexities of a Simple Tissue," 1992–96. https://doi.org/10.1002/stem.534.

[5] Dowthwaite Gary P, Joanna C Bishop, Samantha N Redman, Ilyas M Khan, Paul Rooney, Darrell J R Evans, Laura Haughton, et al. 2004. "The Surface of Articular Cartilage Contains a Progenitor Cell Population" 2 (35 mm). https://doi.org/10.1242/jcs.00912.

[6] Monzón Mario, Rui L Reis, Chaozong Liu, Sara Ajami, Miguel Oliveira, Ricardo Donate, and Viviana Ribeiro. 2018. "Functionally Graded Additive Manufacturing to Achieve Functionality Specifications of Osteochondral Scaffolds." Bio-Design and Manufacturing 1 (1). Springer Singapore: 69–75. https://doi.org/10.1007/s42242-018-0003-4.

[7] Pareek Ayoosh, James L Carey, Patrick J Reardon, Lars Peterson, Michael J Stuart, and Aaron J Krych. 2016. "Long-Term Outcomes after Autologous Chondrocyte Implantation : A Systematic Review at Mean Follow-Up of 11 . 4 Years." https://doi.org/10.1177/1947603516630786.

[8] Mano J F, and R L Reis. 2007. "Osteochondral Defects : Present Situation and Tissue Engineering Approaches," 261–73. https://doi.org/10.1002/term.

[9] Wylde V, P Dieppe, S Hewlett, and I D Learmonth. 2007. "Total Knee Replacement : Is It Really an Effective Procedure for All ?" 14: 417–23. https://doi.org/10.1016/j.knee.2007.06.001.

[10] Darling B. 2005. "The National Joint Registry Annual Report London: Office for public sector information"

[11] Klein Travis J, D Ph, Jos Malda, D Ph, Robert L Sah, D Sc, Dietmar W Hutmacher, and D Ph. 2009. "Tissue Engineering of Articular Cartilage with Biomimetic Zones" 15 (2).

[12] Poole AR. Cartilage in health and disease. In: Koopman WJ, ed. Arthritis and Allied Conditions: A Textbook of Rheumatology. Baltimore: Williams & Wilkins, 1997:255–308

[13] Liao I-chien, Franklin T Moutos, Bradley T Estes, Xuanhe Zhao, and Farshid Guilak. 2013. "Composite Three-Dimensional Woven Scaffolds with Interpenetrating Network Hydrogels to Create Functional Synthetic Articular Cartilage," 5833–39. https://doi.org/10.1002/adfm.201300483.

[14] Swieszkowski Wojciech, Barnabas Ho, Saey Tuan, Krzysztof J Kurzydlowski, and Dietmar W Hutmacher. 2007. "Repair and Regeneration of Osteochondral Defects in the Articular Joints" 24: 489–95. https://doi.org/10.1016/j.bioeng.2007.07.014.

[15] Liao I-chien, Franklin T Moutos, Bradley T Estes, Xuanhe Zhao, and Farshid Guilak. 2013. "Composite Three-Dimensional Woven Scaffolds with Interpenetrating Network Hydrogels to Create Functional Synthetic Articular Cartilage," 5833–39. https://doi.org/10.1002/adfm.201300483.

[16] Luca, Andrea Di, Clemens Van Blitterswijk, and Lorenzo Moroni. 2015. "The Osteochondral Interface as a Gradient Tissue : From Development to the Fabrication of Gradient Scaffolds for Regenerative Medicine." https://doi.org/10.1002/bdrc.21092.

[17] Xiaoming Zhang, Darryl Blalock and Jinxi Wang. 2015. "Classifications and Definitions of Normal Joints, Osteoarthritis - Progress in Basic Research and Treatment," Qian Chen, IntechOpen. https://doi.org/10.5772/59977.

[18] Langer Robert, and Joseph P Vacanti. 1993. "- ARTICLES Tissue Engineering" 260 (May).

[19] USNational Science and Technology Council 2007 Advancing tissue science & engineering: a multi-agency strategic plan available at: (https://whitehouse.gov/sites/default/files/microsites/ostp/advancing_tissue_science-engineering.pdf)

[20] Manufacturing, Additive. 2017. “Three-Dimensional Printing of Tissue / Organ Analogues Containing Living Cells” 45 (1): 180–94. https://doi.org/10.1007/s10439-016-1611-9.

[21] Boland Thomas, Ahu Arslan-yildiz, Rami El Assal, Pu Chen, Dazhong Wu, and Changxue Xu. 2010. “Bioprinting Is Coming of Age : Report from the International Conference on Bioprinting and Biofabrication in Bordeaux (3B ’ 09).” https://doi.org/10.1088/1758-5082/2/1/010201.

[22] Zhao Yu, Rui Yao, Liliang Ouyang, and Hongxu Ding. 2014. “Three-Dimensional Printing of Hela Cells for Cervical Tumor Model in Vitro.” https://doi.org/10.1088/1758-5082/6/3/035001.

[23] Sheth Rahul, Elie R Balesh, Yu Shrike Zhang, Joshua A Hirsch, Ali Khademhosseini, and Rahmi Oklu. n.d. “Three-Dimensional Printing : An Enabling Technology for IR.” https://doi.org/10.1016/j.jvir.2016.02.029.

[24] Zhang Yu Shrike, Margaux Duchamp, Rahmi Oklu, Leif W Ellisen, Ali Khademhosseini, United States, United States, et al. 2017. “HHS Public Access” 2 (10): 1710–21. https://doi.org/10.1021/acsbiomaterials.6b00246.Biopr
inting.

[25] Zhang, Yu Shrike, Kan Yue, Julio Aleman, Kamyar Mollazadeh Moghaddam, Pribpandao Assawes, Su Ryon Shin, Mehmet Remzi Dokmeci, and Rahmi Oklu. 2018. “HHS Public Access” 45 (1): 148–63. https://doi.org/10.1007/s10439-016-1612-8.3D.

[26] Malda Jos, Jetze Visser, Ferry P Melchels, Tomasz Jüngst, Wim E Hennink, Wouter J A Dhert, Jürgen Groll, and Dietmar W Hutmacher. 2013. “25th Anniversary Article : Engineering Hydrogels for Biofabrication,” 5011–28. https://doi.org/10.1002/adma.201302042.

[27] Yoshikawa Hideki, and Norimasa Nakamura. 2014. “Osteochondral Tissue Engineering with Biphasic Scaffold : Current Strategies and Techniques” 20 (5). https://doi.org/10.1089/ten.teb.2013.0543.

[28] Lotz Martin, Darryl D D Lima, and D Ph. 2012. “Direct Human Cartilage Repair Using Three-Dimensional Bioprinting Technology 1,2” 18: 1304–12. https://doi.org/10.1089/ten.tea.2011.0543.

[29] Liu Wanjun, Marcel A Heinrich, Yixiao Zhou, Ali Akpek, Ning Hu, and Xiao Liu. 2017. “Extrusion Bioprinting of Shear-Thinning Gelatin Methacryloyl Bioinks” 1601451: 1–11. https://doi.org/10.1002/adhm.201601451.

[30] Visser Jetze, Benjamin Peters, Byoung Soo Kim, Jinah Jang, Suhun Chae, Alicja Kosik-kozio, Marco Costantini, and Vishakha Grover. n.d. “Bioprinting of Hybrid Tissue Constructs with Tailorable Mechanical Properties.” https://doi.org/10.1088/1758-5082/3/2/021001.

[31] Moroni L, J R De Wijn, and C A Van Blitterswijk. 2006. “3D Fiber-Deposited Scaffolds for Tissue Engineering : Influence of Pores Geometry and Architecture on Dynamic Mechanical Properties” 27: 974–85. https://doi.org/10.1016/j.biomaterials.2005.07.023.

[32] Groll Juergen, Gernot Hochleitner, Tomasz Jüngst, Toby D Brown, Kathrin Hahn, Claus Moseke, and Franz Jakob. 2015. “Additive Manufacturing of Scaffolds with Sub- Micron Filaments via Melt Electrospinning Writing Additive Manufacturing of Scaffolds with Sub-Micron Fi Laments via Melt Electrospinning Writing.” IOP Publishing. https://doi.org/10.1088/1758-5090/7/3/035002.

[33] Brown Toby D, Paul D Dalton, and Dietmar W Hutmacher. 2011. “Direct Writing By Way of Melt Electrospinning,” 5651–57. https://doi.org/10.1002/adma.201103482.

[34] Castilho Miguel, Dries Feyen, María Flandes-iparraguirre, Gernot Hochleitner, Jürgen Groll, Pieter A F Doevendans, Tina Vermonden, Keita Ito, Joost P G Sluijter, and Jos Malda. 2017. “Melt Electrospinning Writing of Poly-Hydroxymethylglycolide- Co - -Caprolactone-Based Scaffolds for Cardiac Tissue Engineering” 1700311: 1–9. https://doi.org/10.1002/adhm.201700311.

[35] Messimer Sherri L, Tais Rocha Pereira, Albert E Patterson, and Maliha Lubna. n.d. “Full-Density Fused Deposition Modeling Dimensional Error as a Function of Raster Angle and Build Orientation : Large Dataset for Eleven Materials.” https://doi.org/10.3390/jmmp3010006.

[36] Perrin DE, English JP. Polycaprolactone. In: Domb AJ, Kost J, Wiseman DM, editors. Handbook of biodegradable polymers. Australia: Harwood Academic; 1998. p 63–77.

[37] Hutmacher Dietmar W, Thorsten Schantz, Iwan Zein, Kee Woei Ng, Swee Hin Teoh, and Kim Cheng Tan. 2001. “Mechanical Properties and Cell Cultural Response of Polycaprolactone Scaffolds Designed and Fabricated via Fused Deposition Modeling,” no. 4.

[38] Onofrillo Carmine, Serena Duchi, D Cathal, O Connell, Nandana Bhardwaj, Onur Bas, Elena M De-juanpardo, Christoph Meinert, Davide D Angella, and Jeremy G Baldwin. 2017. “Biofabricated Soft Network Composites for Cartilage Tissue Engineering Biofabricated Soft Network Composites for Cartilage Tissue Engineering.” IOP Publishing.

[39] Visser Jetze, Ferry P W Melchels, June E Jeon, Erik M Van Bussel, Laura S Kimpton, Helen M Byrne, Wouter J A Dhert, Paul D Dalton, Dietmar W Hutmacher, and Jos Malda. 2015. "Three-Dimensionally Printed Microfibres." Nature Communications. Nature Publishing Group, 1–10. https://doi.org/10.1038/ncomms7933.

[40] J. Mater. Chem. B, 2015, 3, 9067. doi:10.1039/c5tb01645b

[41] Haigh Jodie N, Ya-mi Chuang, Brooke Farrugia, Richard Hoogenboom, Paul D Dalton, and Tim R Dargaville. n.d. "Hierarchically Structured Porous Poly (2-Oxazoline) Hydrogels," 93–99.

[42] Ruijter Mylène De, Alexandre Ribeiro, Inge Dokter, Miguel Castilho, and Jos Malda. 2018. "Simultaneous Micropatterning of Fibrous Meshes and Bioinks for the Fabrication of Living Tissue Constructs" 1800418. https://doi.org/10.1002/adhm.201800418.

[43] Chang Chih-hung, Feng-huei Lin, Chien-cheng Lin, Cheng-hung Chou, and Hwa-chang Liu. 2004. "Cartilage Tissue Engineering on the Surface of a Novel Gelatin – Calcium-Phosphate Biphasic Scaffold in a Double-Chamber Bioreactor," 313–21. https://doi.org/10.1002/jbm.b.30090.

[44] Duan Pingguo, Zhen Pan, Lu Cao, Yao He, Huiren Wang, Zehua Qu, and Jian Dong. 2013. "The Effects of Pore Size in Bilayered Poly (Lactide- Co -Glycolide) Scaffolds on Restoring Osteochondral Defects in Rabbits," no. 973: 180–92.

[45] Solchaga Luis A, Jung U Yoo, Magnus Lundberg, James E Dennis, Barbara A Huibregtse, Victor M Goldberg, and Arnold I Caplan. 2000. "Hyaluronan-Based Polymers in the Treatment of Osteochondral Defects," no. 52: 777–80..

[46] Li Bingyun, and Thomas Webster. n.d. Orthopedic Biomaterials.

[47] Ahn Ji-hyun, Tae-hyeong Lee, Jong-soo Oh, Su-yeon Kim, Hyun-jung Kim, D Ph, Il-kyu Park, Baek-sun Choi, and Gun-ii Im. 2009. "Biphasic Scaffold for the Repair of Osteochondral Defects in Rabbits" 15 (9).

[48] Alluri Ram, Adam Jakus, Sofia Bougioukli, William Pannell, Osamu Sugiyama, Amy Tang, Ramille Shah, and Jay R Lieberman. 2018. "3D Printed Hyperelastic ' Bone ' Scaffolds and Regional Gene Therapy : A Novel Approach to Bone Healing," 1104–10. https://doi.org/10.1002/jbm.a.36310.

[49] Wang Wenhao, and Kelvin W K Yeung. 2017. "Bioactive Materials Bone Grafts and Biomaterials Substitutes for Bone Defect Repair : A Review." Bioactive Materials 2 (4). Elsevier Ltd: 224–47. https://doi.org/10.1016/j.bioactmat.2017.05.007.

[50] Jakus Adam E, Alexandra L Rutz, Sumanas W Jordan, Abhishek Kannan, Sean M Mitchell, Chawon Yun, Katie D Koube, et al. 2016. "Hyperelastic ' Bone ' : A Highly Versatile , Growth Factor – Free , Osteoregenerative , Scalable , and Surgically Friendly Biomaterial" 8 (358): 1–16.

[51] Spiller Kara, Jonathan Bernhard, and Gordana Vunjak-novakovic. 2017. "Biomimetic Approaches for Bone Tissue Engineering 1 2 1" 23 (5): 480–93. https://doi.org/10.1089/ten.teb.2016.0289.

[52] Li Jiao Jiao, Mohamed Ebied, Jen Xu, and Hala Zreiqat. 2018. "Current Approaches to Bone Tissue Engineering : The Interface between Biology and Engineering" 1701061: 1–8. https://doi.org/10.1002/adhm.201701061.

[53] Shao Xinxin, James C H Goh, Dietmar W Hutmacher, E N G H I N Lee, and G E Zigang. 2006. "Repair of Large Articular Osteochondral Defects Using Hybrid Scaffolds and Bone Marrow-Derived Mesenchymal Stem Cells" 12 (6).

[54] Miar Solaleh, Ashkan Shafiee, Teja Guda, and Roger Narayan. 2018. Additive Manufacturing for Tissue Engineering.

[55] Nooeaid Patcharakamon, Vehid Salih, Justus P Beier, and Aldo R Boccaccini. 2012. "Osteochondral Tissue Engineering : Scaffolds , Stem Cells and Applications Scaffolds for Osteochondral Tissue Engineering" 16 (10): 2247–70. https://doi.org/10.1111/j.1582-4934.2012.01571.x.

[56] Harley Brendan A, Andrew K Lynn, Zachary Wissner-gross, William Bonfield, Ioannis V Yannas, and Lorna J Gibson. 2009. "Design of a Multiphase Osteochondral Scaffold III : Fabrication of Layered Scaffolds with Continuous Interfaces." https://doi.org/10.1002/jbm.a.32387.

[57] Cao Tong, D Ph, Kee-hai Ho, Swee-hin Teoh, and D Ph. 2003. "Scaffold Design and in Vitro Study of Osteochondral Coculture in a Three-Dimensional Porous Polycaprolactone Scaffold Fabricated by Fused Deposition Modeling" 9.

[58] Ã Savio L Woo, Steven D Abramowitch, Robert Kilger, and Rui Liang. 2006. "Biomechanics of Knee Ligaments : Injury , Healing , and Repair" 39: 1–20. https://doi.org/10.1016/j.jbiomech.2004.10.025.

[59] Sittinger Michael, Perka Carsten, Schultz Olaf, Haupl Thomas, Burmester Gerd R. 1999. "Joint cartilage regeneration by tissue engineering," 58(3):130-135

[60] Anatomical A Comparative, Study Of, T H E Human, and S I X Animal Species. 2013. "A COMPARATIVE ANATOMICAL STUDY OF THE HUMAN KNEE" 19 (4): 493–99. https://doi.org/10.1016/j.knee.2011.07.005.A.

[61] Patil Shantanu, Nikolai Steklov, Lin Song, Won C Bae, and Darryl D D Lima. 2014. "The Knee Comparative Biomechanical Analysis of Human and Caprine Knee Articular Cartilage." The Knee 21 (1). Elsevier B.V.: 119–25. https://doi.org/10.1016/j.knee.2013.03.009.

[62] Grood S, Skin Diseases, and Noyes-giannestras Biomechanics Laboratories. 1994. "IN VI ?‘ 0 FORCES IN THE ANTERIOR CRUCIATE LIGAMENT : DIRECT MEASUREMENTS DURING WALKING" 21 (5).

[63] Perry, Editors Jacquelin, and Judith M Burnfield. 2010. "Gait Analysis : Normal and Pathological Function," 2010.

[64] Chhabra Avneesh, Starman JS, Ferretti Marcos, Vidal AF, Zantop Thore, Freddie H Fu. 2006. "Anatomic, radiographic, biomechanical, and kinematic evaluation of the anterior cruciate ligament and its two functional bundles," 88(Suppl 4):2–10. doi:10.2106/ JBJS.F.00616

[65] Steckel H, J S Starman, M H Baums, H M Klinger, W Schultz, and F H Fu. 2007. "The Double-Bundle Technique for Anterior Cruciate Ligament Reconstruction : A Systematic Overview," 99–108. https://doi.org/10.1111/j.1600-0838.2006.00600.x.

[66] Ronga M, Muriuki M, Ekdahl M, Smolinski P, Fu FH. 2008. "Anatomical description of the anterior cruciate ligament in goat knee," 16:S42123

[67] Zantop Thore, Mirko Herbort, Michael J Raschke, Freddie H Fu, and Wolf Petersen. n.d. "The Role of the Anteromedial and Posterolateral Bundles of the Anterior Cruciate Ligament in Anterior Tibial Translation and Internal Rotation," 223–27. https://doi.org/10.1177/0363546506294571.

[68] Smolinski P, M Ekdahl, and Freddie H Fu. 2009. "Biomechanics of the Goat Three Bundle Anterior Cruciate Ligament," 935–40. https://doi.org/10.1007/s00167-009-0784-2.

[69] Tapper Janet E, Shige Fukushima, Hiro Azuma, Gail M Thornton, Janet L Ronsky, Nigel G Shrive, and Cyril B Frank. 2006. "Dynamic In Vivo Kinematics of the Intact Ovine Stifle Joint," no. April: 782–92. https://doi.org/10.1002/jor.

[70] Little C B, M M Smith, M A Cake, R A Read, M J Murphy, and F P Barry. 2010. "The OARSI Histopathology Initiative E Recommendations for Histological Assessments of Osteoarthritis in Sheep and Goats" 18: 80–92. https://doi.org/10.1016/j.joca.2010.04.016.

[71] Takroni Talal, Leila Laouar, Adetola Adesida, Janet A W Elliott, and Nadr M Jomha. 2016. "Anatomical Study : Comparing the Human , Sheep and Pig Knee Meniscus." Journal of Experimental Orthopaedics. Journal of Experimental Orthopaedics. https://doi.org/10.1186/s40634-016-0071-3.

[72] Osterhoff Georg, Sabine Löf, Hanno Steinke, Christine Feja, Christoph Josten, and Pierre Hepp. 2011. "The Knee Comparative Anatomical Measurements of Osseous Structures in the Ovine and Human Knee" 18: 98–103. https://doi.org/10.1016/j.knee.2010.02.001.

[73] Radford W.J.P., Amis A.A., Stead A.C. 1996. The Ovine Stifle as a Model for Human Cruciate Ligament Surgery.

[74] Taylor, William R, Rainald M Ehrig, Markus O Heller, Hanna Schell, Petra Seebeck, and Georg N Duda Ã. 2006. "Tibio-Femoral Joint Contact Forces in Sheep" 39: 791–98. https://doi.org/10.1016/j.jbiomech.2005.02.006.

[75] Wu Dan, Per Isaksson, Stephen J Ferguson, and Cecilia Persson. 2018. "Young ' S Modulus of Trabecular Bone at the Tissue Level : A Review." Acta Biomaterialia, no. August. Acta Materialia Inc. https://doi.org/10.1016/j.actbio.2018.08.001.

[76] Castilho Miguel, Vivian Mouser, Mike Chen, Jos Malda, and Keita Ito. 2019. "Bi-Layered Micro-Fibre Reinforced Hydrogels for Articular Cartilage Regeneration." Acta Biomaterialia. Acta Materialia Inc. https://doi.org/10.1016/j.actbio.2019.06.030.

Appendices

1.1 Convergence of MEW and extrusion-based techniques



1.2 CT-scan data of the volume of the bulk HB scaffold



1.3 Spontaneous removal of culture medium under compression

